Constraining urban fossil fuel CO_2 emissions in Seoul using combined ground and satellite observations with Bayesian inverse modelling

Sojung Sim[1,2], Sujong Jeong[2,3]

[1]Environmental Planning Institute, Seoul National University, Seoul, 08826, Republic of Korea
[2]Climate Tech Center, Seoul National University, Seoul, 08826, Republic of Korea
[3]Department of Environmental Management, Graduate School of Environmental Studies, Seoul National University, Seoul, 08826, Republic of Korea

Correspondence to: Sujong Jeong (sujong@snu.ac.kr)

Abstract. Accurate carbon emission estimates are essential for achieving net zero targets by 2050. The Bayesian inverse method, combined with atmospheric carbon dioxide (CO_2) measurements and a transport model, can serve as an independent verification approach to improve accuracy. We developed a Bayesian inverse modelling framework using ground- and space-based measurements and applied it to Seoul to test the framework and constrain its fossil fuel CO_2 emissions. By leveraging the high temporal resolution of ground-based in situ observations and the broad spatial coverage of satellite data, we improved the accuracy of emission estimates. Our results indicate the spatiotemporal variability of posterior emissions increased significantly, enabling us to track CO_2 fluctuations and assess the impact of carbon reduction policies over time and space. The mean absolute error between simulated and observed CO_2 enhancements decreased by 55%, indicating improved agreement. We investigated the performance of the inverse model through a sensitivity analysis that considered different observational network configurations. Uncertainty reductions varied with the type of observations used: 19.2% when all observations were included, 18.7% using only ground-based sites, and 6–8.4% when using only OCO-2 or OCO-3 satellite data, highlighting the complementary contributions of ground and space-based measurements. The analysis also showed that assumptions about background concentrations, biogenic fluxes, and prior emission uncertainties can alter posterior results, demonstrating the importance of model configuration. The framework shows strong potential for application in other cities and can support the development of effective climate mitigation policies.

Graphical abstracts

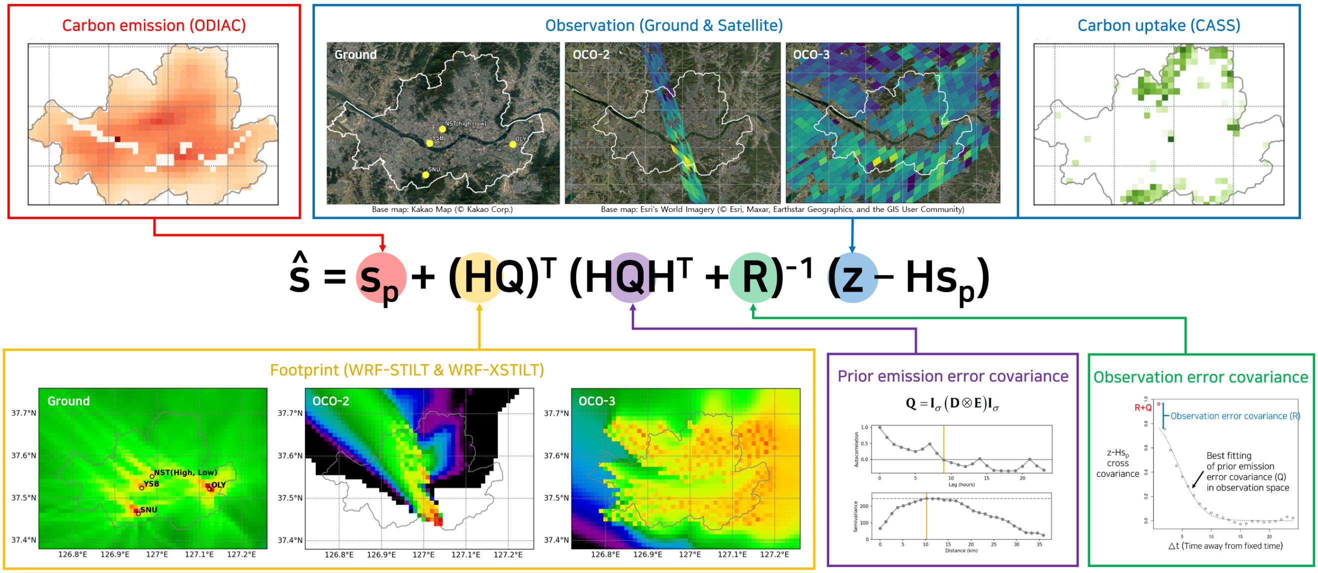

1 Introduction

Global carbon emissions from fossil fuel combustion and land-use change are redistributed among the atmosphere, ocean, and land (Friedlingstein et al., 2022). In the global carbon cycle, these five major components closely interact to maintain balance. However, anthropogenic emissions of greenhouse gases (GHGs), particularly carbon dioxide (CO_2), have dominated since the industrial era, resulting in rising atmospheric CO_2 levels and driving climate change (Friedlingstein et al., 2022). Human-caused climate change amplifies global surface temperatures and impacts weather extremes such as heatwaves, tropical cyclones, droughts, and heavy precipitation (IPCC, 2023). To mitigate the adverse effects of climate change worldwide, international climate agreements like the United Nations Framework Convention on Climate Change, the Kyoto Protocol, and the Paris Agreement have been implemented (IPCC, 2023). The IPCC 1.5℃ Special Report declared that achieving global net-zero CO_2 emissions by 2050 is imperative to limit the increase in global temperature to 1.5 °C above pre-industrial levels (IPCC, 2018). More than 130 countries have signalled an intention to reduce CO_2 emissions to near net-zero by around mid-century (Robinson and Shine, 2018).

By 2050, 68% of the world's population is projected to reside in urban areas (UN-DESA, 2018). At least 70% of global anthropogenic CO_2 emissions originate from cities (IEA, 2015). Given the concentration of population and CO_2 emissions in cities, they bear significant responsibility for emission reduction and are expected to play a major role in meeting their net-zero goals. The C40 Climate Leadership Group, comprising around 100 cities worldwide, has pledged to reduce GHG emissions and developed a science-based approach (C40 Cities, 2022). To support urban emission reduction strategies, the quality assurance of CO_2 emission estimates is required (Gurney et al., 2021; IPCC, 2019). Accurate emission estimates can provide detailed guidance to establish a baseline for prioritizing climate action and assessing policy progress over time (Mueller et al., 2021).

Various efforts are underway to estimate CO_2 emissions through a bottom-up approach. This approach calculates anthropogenic CO_2 emissions based on socio-economic databases (e.g., energy consumption, housing statistics, and road networks) and emission factors. The Global Protocol for Community-Scale Greenhouse Gas Emission Inventories (GPC) provides a standardized framework adopted by major city networks such as C40 Cities (WRI et al., 2014). It offers consistent accounting methods for different emission sectors within urban boundaries, enabling cities worldwide to compile self-reported emission inventories. However, these inventories are typically reported at an annual scale, resulting in low spatial and temporal resolution. Because of limited access to activity data and unknown emission factors within urban areas, detailed CO_2 emission estimates with high spatial and temporal resolution have been developed only for certain cities, such as Indianapolis (Gurney et al., 2012), Los Angeles (Feng et al., 2016; Gurney et al., 2019b), Salt Lake City (Patarasuk et al., 2016), and New York (Gately et al., 2015). Other types of emission data products, including CDIAC (Carbon Dioxide Information and Analysis Center), EDGAR (Emissions Database for Global Atmospheric Research), and ODIAC (Open-Data Inventory for Anthropogenic Carbon Dioxide), have been devised to downscale global/national total emission estimates using proxies such as nighttime lights and population. However, large discrepancies have been reported between bottom-up and GPC-based inventories and downscaled CO_2 datasets at the urban scale. These differences arise from variations in emission sources (e.g., large point sources and road traffic), outdated local-specific emission factors, and inconsistencies in spatial or temporal coverage (Ahn et al., 2023; Gurney et al., 2019a; Palermo et al., 2024). Such uncertainties limit the establishment of a CO_2 emissions baseline and assessing mitigation outcomes at the city levels.

A complementary and independent approach to verify these CO_2 emission estimates is deemed necessary (IPCC, 2019). In the top-down approach, emission estimates can be constrained via real-time CO_2 measurements and atmospheric transport models. Consequently, combining bottom-up and top-down estimates has been explored using a Bayesian inversion approach for accurate CO_2 emission estimation. Bayesian inversion approach has been used in recent studies to optimize existing bottom-up estimates over Salt Lake City (Kunik et al., 2019; Mallia et al., 2020), Paris (Lian et al., 2022; Nalini et al., 2022), Los Angeles (Ye et al., 2020), and Tokyo (Ohyama et al., 2023; Pisso et al., 2019). They obtained optimal CO_2 emissions with uncertainty reductions of 39.32% (Kunik et al., 2019), 27.7% (Mallia et al., 2020), 8–10% (Lian et al., 2022), 2–10% (Nalini et al., 2022), ~50% (Ohyama et al., 2023), and 20.09% (Pisso et al., 2019) compared to prior emissions. ()

Previous studies that performed inverse modelling for urban areas have primarily relied on a single type of observation to constrain emissions, most commonly ground-based in situ CO_2 measurements (Breón et al., 2015; Göckede et al., 2010; Lauvaux et al., 2016; Lian et al., 2023, 2022; Mallia et al., 2020; McKain et al., 2012; Nalini et al., 2022; Sargent et al., 2018; Staufer et al., 2016). Some studies have instead used ground-based Fourier Transform Infrared (FTIR) column-averaged CO_2 (XCO_2) observations (Hedelius et al., 2018; Ohyama et al., 2023), airborne observations (Lopez-Coto et al., 2020; Pitt et al., 2022), or satellite observations (Hamilton et al., 2024; Kaminski et al., 2022; Roten et al., 2023; Wu et al., 2018; Ye et al., 2020). However, studies that combine multiple observation types to leverage their complementary strengths remain rare. Although Pisso et al. (2019) integrated in situ airborne and ground-based observations to assess Lagrangian inverse modelling, and Che et al. (2024) combined ground-based FTIR and satellite data to estimate CO_2 emissions, these studies focused on either near-surface CO_2 concentrations or vertical CO_2 profiles, rather than incorporating both perspectives. In this study, we integrate ground-based in situ CO_2 observations, which provide detailed information on surface emissions and uptake with high temporal resolution, and satellite observations, which offer broad spatial coverage and capture the total atmospheric CO_2 column. By combining these two complementary datasets, we simultaneously account for surface CO_2 fluxes and their impact on the vertical distribution of atmospheric CO_2. To our knowledge, this is the first inverse modelling study to fully utilize surface and column-integrated CO_2 measurements, providing a more comprehensive constraint on urban CO_2 emissions.

Seoul is a megacity with a population of approximately 10 million, which accounts for 18% of South Korea's total population in 2022 (KOSIS, 2023). The population and infrastructure in Seoul are densely concentrated, making it more susceptible to severe damage from climate change than other regions. It also has one of the highest carbon emissions among the 13,000 cities worldwide (Moran et al., 2018). Seoul has participated in the C40 Climate Leadership Group since 2006, and in 2020, it announced the '2050 GHGs Reduction Promotion Plan' to achieve a net-zero emissions goal (Seoul Metropolitan Government, 2021). Within Seoul, a comprehensive CO_2 monitoring network has been established, encompassing numerous stationary monitoring sites and mobile platforms to understand the urban carbon cycle (Park et al., 2020; Sim et al., 2020). Given its dense population, concentrated emissions, and extensive measurement networks, Seoul can be an optimal testbed city for studies to verify CO_2 emission estimates and assess the effectiveness of the CO_2 monitoring network.

In this study, we used a Bayesian inverse model and ground- and space-based measurements to improve the accuracy of CO_2 emission estimates over Seoul. We developed a high-resolution Bayesian inverse modelling framework with a spatial resolution of 0.01° (approximately 1 km) and a temporal resolution of 1 h, incorporating anthropogenic CO_2 emissions, biogenic CO_2 fluxes, atmospheric CO_2 measurements, a Lagrangian transport model, and error covariances of both prior emissions and observations. We then estimated the optimal spatiotemporal distribution of CO_2 emissions over Seoul for December 2021, verifying existing emission data. Additionally, we evaluated the effectiveness of the inversion by comparing observed and simulated CO_2 enhancements using prior and posterior emissions. Finally, we conducted sensitivity tests on different observational datasets and input assumptions to assess their impact on emission estimates.

2 Data and methods

2.1 Bayesian inverse method

In this study, data assimilation is employed to estimate optimal (posterior) CO_2 emissions close to the true emissions. Data assimilation in CO_2 estimation optimally combines information from atmospheric CO_2 observations with a transport model and prior CO_2 emissions to produce accurate posterior estimates of CO_2 emissions. Posterior CO_2 emissions are derived through the minimization of the cost function (Enting, 2002; Tarantola, 1987) defined as follows:

$$\boldsymbol{L_s} = \frac{1}{2}(\boldsymbol{z} - \boldsymbol{Hs})^{\boldsymbol{T}}\boldsymbol{R}^{-1}(\boldsymbol{z} - \boldsymbol{Hs}) + \frac{1}{2}\left(\boldsymbol{s} - \boldsymbol{s_p}\right)^{\boldsymbol{T}}\boldsymbol{Q}^{-1}(\boldsymbol{s} - \boldsymbol{s_p}) \tag{1}$$

Where $\boldsymbol{z}$ is a vector of observed CO_2 enhancements, $\boldsymbol{H}$ is the Jacobian matrix of footprint values from the atmospheric transport model, $\boldsymbol{s}$ is a vector of the unknown true CO_2 emissions, $\boldsymbol{R}$ is the covariance of observational errors, $\boldsymbol{s_p}$ is a state vector of prior CO_2 emissions, and $\mathbf{Q}$ is the covariance of prior emission errors. The solution obtained by minimizing the cost function defined in Eq. (1) yields the optimized posterior CO_2 emission estimates ($\hat{s}$), expressed as:

$$\hat{\boldsymbol{s}} = \boldsymbol{s_p} + (\boldsymbol{HQ})^{\boldsymbol{T}}(\boldsymbol{HQH^T} + \boldsymbol{R})^{-1}(\boldsymbol{z} - \boldsymbol{Hs_p}) \tag{2}$$

The posterior uncertainty covariance ($\boldsymbol{V_{\hat{s}}}$) can be expressed as:

$$\boldsymbol{V_{\hat{s}}} = \boldsymbol{Q} - (\boldsymbol{HQ})^{\boldsymbol{T}}(\boldsymbol{HQH^T} + \boldsymbol{R})^{-1}(\boldsymbol{HQ}) \tag{3}$$

Using the posterior uncertainty covariance obtained from Eq. (3), the reduction in uncertainty resulting from the constraints on emissions can be quantified. The uncertatinty reduction (UR) is defined as:

$$\boldsymbol{UR} = \frac{\sqrt{\boldsymbol{Q_{tot}}} - \sqrt{\boldsymbol{V_{\hat{s}\_tot}}}}{\sqrt{\boldsymbol{Q_{tot}}}} \times \mathbf{100\%} \tag{4}$$

Here, $\boldsymbol{Q_{tot}}$ represents the domain- and time-averaged covariance of prior emission errors and $\boldsymbol{V_{\hat{s}\_tot}}$ represents the domain- and time-averaged covariance of posterior emission errors.

In this study, we assessed the validity of posterior emissions resulting from the inverse model by calculating the reduced chi-squared value ($\boldsymbol{\chi_r^2}$) following Tarantola (1987). It is computed using the equation:

$$\boldsymbol{\chi_r^2} = \frac{\mathbf{1}}{\boldsymbol{v}}[(\mathbf{z} - \mathbf{H}\hat{\mathbf{s}})^{\boldsymbol{T}}\boldsymbol{R}^{-1}(\boldsymbol{z} - \boldsymbol{H\hat{s}}) + (\hat{\boldsymbol{s}} - \boldsymbol{s_p})^{\boldsymbol{T}}\boldsymbol{Q}^{-1}(\hat{\boldsymbol{s}} - \boldsymbol{s_p})] \tag{5}$$

Where the squared data residual ($\mathbf{z} - \mathbf{H}\hat{\mathbf{s}}$) and emissions residual ($\hat{\boldsymbol{s}} - \boldsymbol{s_p}$) from the inversion are normalized by their respective variance matrices, $\boldsymbol{R}$ and $\mathbf{Q}$. The residuals are expected to follow a chi-squared distribution with ν degrees of freedom, which in this study corresponds to the number of observations. The closer the reduced chi-squared value is to 1, the more accurately the prescribed errors of observations and prior emissions are set, leading to a more reliable estimation of posterior emissions.

2.2 Observations

A set of measurements from ground-based and satellite observations, all collected during December 2021, was selected to obtain atmospheric CO_2 concentrations in Seoul. The year 2021 was chosen because it was the first year when CO_2 data from all ground-based observation sites in Seoul became available. December was further selected to minimize the influence of biogenic activity on the inversion results and because both OCO-2 and OCO-3 satellites passed over Seoul during this period, enabling consistent integration of ground-based and satellite observations. Ground-based observations provide continuous, real-time measurements of atmospheric CO_2 at specific locations, whereas satellite observations offer broader spatial coverage that complements the ground network.

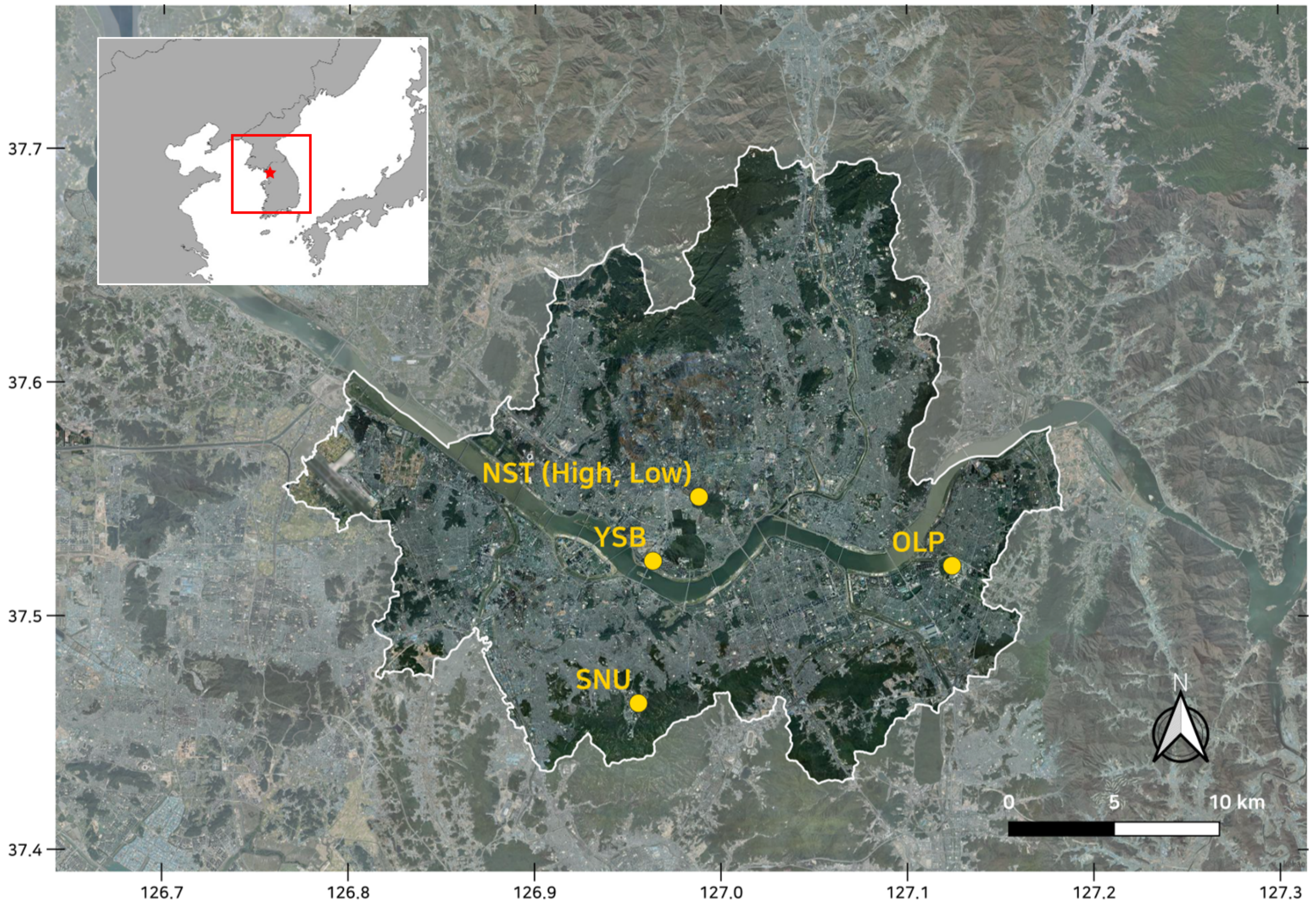

Figure 1: Map of Seoul with the locations of CO_2 ground observation sites: Namsan Tower-high (NST_H), Namsan Tower-low (NST_L), Olympic Park (OLP), Seoul National University (SNU), and Yongsan Building (YSB). Observation sites are denoted with yellow points. The city's elevation generally ranges from 20 to 80 m above sea level, with higher terrain in the northern and southern mountainous areas. The background map is sourced from Kakao Map (© Kakao Corp.). The red box in the inset figure at the upper left indicates the background domain used for satellite-based observations.

For the ground measurements, we used observed CO_2 concentrations from five different sites in Seoul (Park et al., 2021): Namsan Seoul Tower-High (NST_H), Namsan Seoul Tower-Low (NST_L), Olympic Park (OLP), Seoul National University (SNU), and Yongsan Building (YSB), as shown in Fig. 1. The instrument inlet heights of NST_H, NST_L, OLP, SNU, and YSB, combined with the site altitude, are 420, 265, 27, 173, and 113 m above sea level, respectively. The observation instruments installed at NST_L and OLP are PICARRO's G2301, whereas those installed at NST_H, SNU, and YSB are LICOR's LI-850. We utilized only daytime data (10:00–16:00 KST) for the inverse modelling to minimize the impact of model biases in the planetary boundary layer (PBL) height. The CO_2 concentrations measured at each ground observation site exhibit different patterns of variation because of differences in altitudes and surrounding environments (Fig. 2a). The average daytime CO_2

concentrations at NST_H, NST_L, OLP, SNU, and YSB were 453.7 ± 19.6, 460.1 ± 27.1, 460.2 ± 26.7, 461.5 ± 26.6, and 466.9 ± 31.4 ppm, respectively (Fig. 2b). The lowest average concentration at NST_H is attributed to its location at the top of the tall tower, whereas the highest average concentration at YSB is because of its location in a commercial area with high vehicle traffic. Most observation sites exhibited a typical diurnal pattern of CO_2 concentrations (Fig. 2c), characterized by an increase in the morning as emissions rise (Fig. S4b), followed by a pronounced decrease during the daytime when the PBL height increases and atmospheric mixing becomes more active. At night, although emissions are relatively lower, the shallow PBL leads to an accumulation of CO_2 near the surface, resulting in higher concentrations. However, at the NST_H site, CO_2 concentrations tended to decrease at night, showing an opposite pattern compared to the other sites. This is because the observation inlet at NST_H is often located above the nocturnal PBL, allowing it to be influenced by air masses transported from outside Seoul (Park et al., 2022).

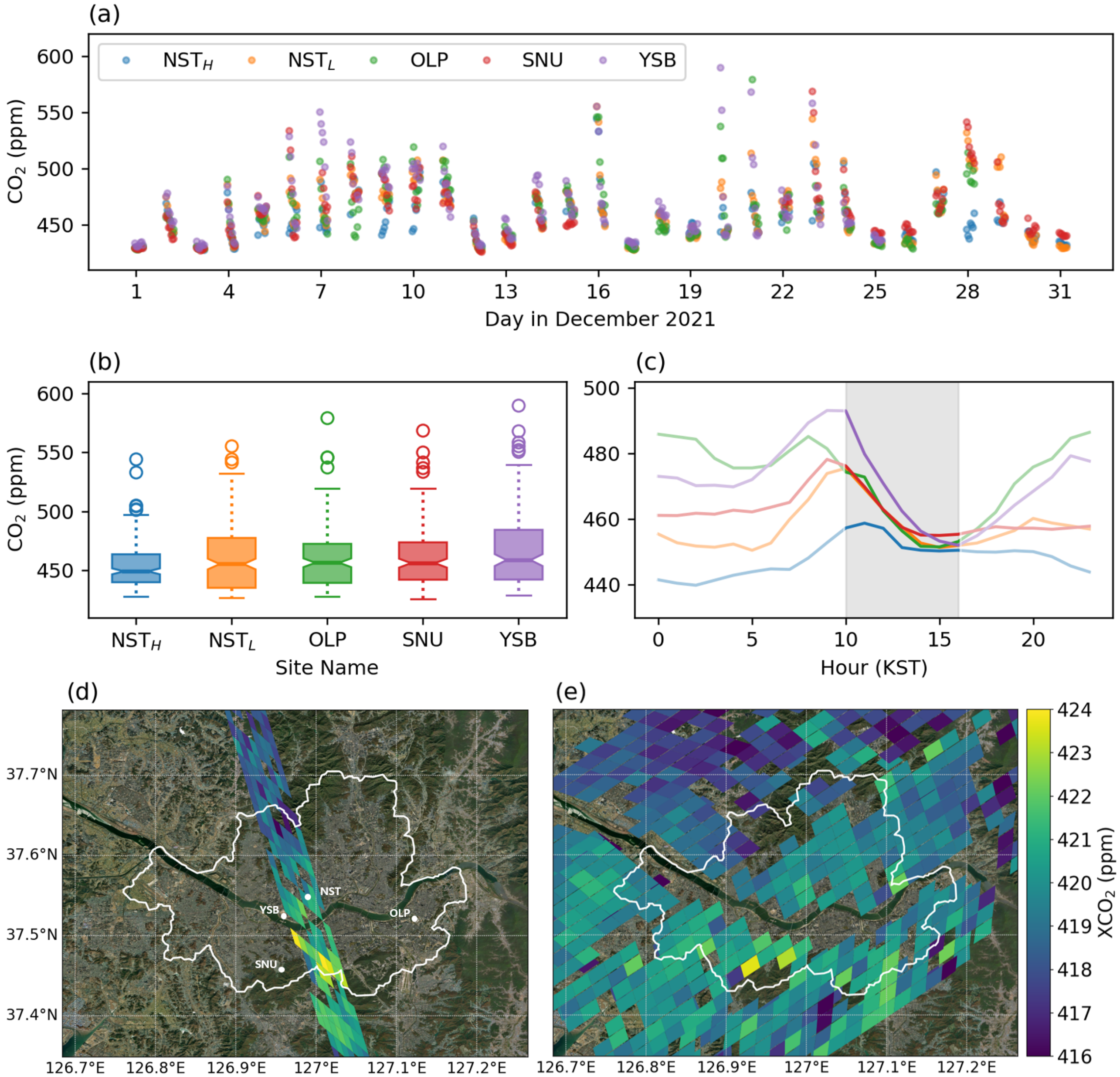

Figure 2: Observation data used in the Bayesian inverse modelling framework over Seoul during December 2021. (a) Time series of daytime (10:00–16:00 KST) CO$_2$ concentrations measured at five ground sites. (b) Box plots of daytime CO$_2$ concentrations from the ground sites. (c) Average diurnal cycles at each site, with gray shaded regions indicating the daytime period. Spatial distributions of XCO$_2$ measured by (d) OCO-2 on December 4, 2021, at 13:00 KST and (e) OCO-3 on December 5, 2021, at 11:00 KST. White circles in panel (d) indicate the locations of the ground observaton sites. The background maps in (d) and (e) are based on Esri's World Imagery (© Esri, Maxar, Earthstar Geographics, and the GIS User Community).

We used satellite measurements from the Orbiting Carbon Observatory-2 (OCO-2) and Orbiting Carbon Observatory-3 (OCO-3) missions. OCO-2 and OCO-3, launched on July 2, 2014, and May 4, 2019, respectively, measure the dry-air column-averaged mole fraction of CO_2 (XCO_2). Both satellites provide high-precision spaceborne observations at a fine spatial resolution, making them highly suitable for urban-scale inverse modelling. In particular, OCO-3 offers the Snapshot Area Mapping mode, specifically designed to detect anthropogenic CO_2 emissions and spatial gradients in densely populated urban environments (Kiel et al., 2021). These capabilities make both satellites valuable for constraining urban CO_2 emissions. Over Seoul, valid OCO-2 and OCO-3 soundings have been intermittently obtained, with data availability varying by month. In 2021, no valid observations were available in February, March, April, August, and September. Only OCO-2 passed over Seoul in July and November, while only OCO-3 provided soundings in January, May, and June. Both satellites observed Seoul in October and December. Among these, December 2021 offered broader spatial coverage and higher-quality retrievals, and was therefore selected for this study. On December 4 and 5, 2021, the OCO-2 and OCO-3 satellites passed over Seoul at 13:00 and 11:00 KST, respectively, yielding 60 and 167 soundings (Figs. 2d and 2e). Only good-quality data were considered when processing the XCO_2 data for observational input in inverse modelling. In both datasets, the XCO_2 values were higher in the southern part of Seoul compared to the northern part. This spatial gradient likely reflects differences in topography and emission patterns. The northern boundary of Seoul is mountainous, resulting in lower XCO_2 levels due to limited anthropogenic activity, whereas the southern part contains densely populated residential and commercial zones with higher emission intensities.

The vector of observed CO_2 enhancements, denoted as **z** in Eq. (1), represents the ΔCO_2 affected by nearby emission sources. Because we aim to optimize Seoul's CO_2 emissions using atmospheric observations, we must calculate ΔCO_2 influenced only by anthropogenic emissions within Seoul, excluding the effects of biogenic fluxes and background. To obtain the ΔCO_2, the vegetation-affected and background concentrations must be subtracted from the observed CO_2 concentrations. The calculation method for the vegetation-affected concentration is described in Sect. 2.4.

To isolate ΔCO_2 from observed CO_2 concentrations at ground observation sites, we determined suitable background representations for the Seoul region. Previous studies have proposed several approaches to estimate background concentrations, including the use of data from background sites, upwind sites, or the observation sites themselves. When background sites are utilized, various data selection strategies have been applied, such as using hourly measurements from high-altitude stations (Nalini et al., 2022), daily minimum values (Fasoli et al., 2018; Zhao et al., 2009), the daily 5th percentile (Ohyama et al., 2023), curve-fitted data (Thoning et al., 1989), or data processed with the Robust Extraction of Baseline Signal algorithm (Ruckstuhl et al., 2012). In approaches considering wind direction, background concentrations have been represented by hourly mixing ratios (Lian et al., 2022; Nalini et al., 2022) or by two-day moving averages of ΔCO_2 from an upwind site (McKain et al., 2012). When background or upwind stations are unavailable, background concentrations can be derived directly from site-specific observations using statistical methods, such as the 24-hour moving 5th percentile (Chandra et al., 2016; Gamage et al., 2020) or the 3-day moving 5th percentile (Ammoura et al., 2014). For the background representation for ground-based observations in Seoul, we calculated observed ΔCO_2 at each site using three approaches: 1) the daily 5th percentile at NST_H, a high-altitude urban background site (denoted as GM1); 2) the 24-hour moving 5th percentile (GM2); and 3) the 3-day moving 5th percentile (GM3), both derived from data at each site. Among these methods, GM2 yielded the lowest mean absolute error (MAE) between observed and modelled ΔCO_2 from posterior emissions and was therefore selected as the reference configuration. The sensitivity of inversion results to different ground background estimation methods is discussed in Section 3.3.2.

To define the background for satellite-based observations, various approaches have also been proposed in previous studies, ranging from simple statistical to geographic and model-based methods, depending on study objectives. Hakkarainen et al. (2016) and Silva and Arellano (2017) employed simple statistical approaches, defining the daily median of all observations within a broad domain or the mean minus one standard deviation of all observations within the target urban area, respectively. However, these domain-wide statistical methods may yield background concentrations that represent a mixture of regions with distinct characteristics. To address this limitation, several studies incorporated geographic information to identify rural regions and used observations from these regions to define background levels. For instance, Kort et al. (2013) and Schneising et al. (2013) utilized data over rural or desert regions with relatively low emissions, while Labzovskii et al. (2019) and Park et al. (2021) defined a ~500,000 km^2 background box centered on each city and used the daily median XCO_2 values over rural areas and their 10 km buffer zones, identified using MODIS land cover data, as the background concentration. Model-based approaches have also been widely adopted. Janardanan et al. (2016) used an atmospheric transport model and flux data to identify grid cells where the simulated anthropogenic signal was below a specified threshold, averaging the corresponding concentrations to define the background. Wu et al. (2018) compared trajectory-endpoint and overpass-specific background methods using a transport model and found that the overpass-specific method was most suitable for capturing local-scale XCO_2 anomalies. They also reported that reducing the spatial domain from 4° × 4° to 2° × 2° in the Silva and Arellano (2017) method yielded results comparable to those from the overpass-specific approach in both variability and magnitude. Similarly, Hamilton et al. (2024) used a transport model to identify upwind regions within the study domain and defined the mean XCO_2 over those regions as the background concentration. Among these various satellite background estimation methods, we selected three representative approaches for this study: 1) a simple statistical method (SM1), following Silva and Arellano (2017); 2) a geographic method (SM2), following Labzovskii et al. (2019) and Park et al. (2021); and 3) a model-based upwind method (SM3), following Hamilton et al. (2024). In SM1, we adopted a 2° × 2° domain centered on Seoul, modifying the original approach based on the recommendation of Wu et al. (2018), and defined the background as the mean minus one standard deviation of all satellite observations within the domain. In SM2, the background was calculated as the daily median XCO_2 over non-urban areas within a ~500,000 km^2 background box centered on Seoul (Fig. 1). Instead of MODIS land cover data used in previous studies, we utilized the land cover map from the Environmental Geographic Information Service (EGIS) of the Ministry of Environment Korea, which more accurately represents domestic geographic conditions (see Text S1 and Fig. S1 in the supplementary material). For SM3, we used a transport model (Section 2.3) to identify upwind regions and defined the mean XCO_2 observed in those regions as the background concentration. Each of the three methods was applied separately to OCO-2 and OCO-3 observations, followed by inverse modelling for sensitivity analyses (Section 3.3.2). Among these, SM2 produced the lowest MAE between observed and modelled ΔCO_2 from posterior emissions and was therefore selected as the reference configuration for this study.

2.3 Atmospheric Transport

The Weather Research and Forecasting model (WRF) with the (X-)Stochastic Time-Inverted Lagrangian Transport (WRF-(X)STILT) was used to derive the Jacobian matrix of footprint values ($\boldsymbol{H}$) at a fine spatial resolution (e.g., 0.01°). We employed the STILT model (Fasoli et al., 2018; Lin et al., 2003) for ground-based observations and X-STILT (Wu et al., 2018) for satellite observations, both driven by meteorological fields from WRF model version 3.9.1 (Skamarock and Klemp, 2008). WRF-(X)STILT is an effective tool for simulating realistic atmospheric transport using a Lagrangian particle dispersion model within the planetary boundary layer (Nehrkorn et al., 2010). Previous studies have widely used WRF-(X)STILT as an atmospheric transport model for applying GHG inverse modelling in urban areas (Kunik et al., 2019; McKain et al., 2012; Ohyama et al., 2023; Sargent et al., 2018; Wu et al., 2018; Zhao et al., 2009).

The model releases backward 3D virtual air particle trajectories with stochastically turbulent dispersion from the observation location (receptor) to potential source regions that influence the receptor. It then counts the dispersed air particles (footprints) in each grid. Footprints quantify the sensitivity of the observation to upstream source regions. They can be regarded as the average contribution of the surface flux at the receptor, as they represent how densely and how long the air particles lingered backward in time within each discretized volume of the upwind source regions. In Bayesian inverse modelling, the footprint acts as an operator, connecting individual CO_2 observations (unit: ppm) and gridded fluxes (unit: $\mu mol/(m^2\ s)$). Using footprints representing concentration per unit flux allows direct comparison between CO_2 emissions and atmospheric CO_2 enhancements. To ensure the reliability of the meteorological inputs used for the inversion, the modelled wind fields from the WRF simulation were evaluated against observational data from the Automated Surface Observing System (ASOS) and Automatic Weather Stations (AWS) operated by the Korea Meteorological Administration. Several sensitivity cases were tested to assess the effects of meteorological inputs, land-use data, and grid nudging on model performance. The mean wind speed bias in Seoul decreased from 2.38 m/s (WRF default configuration) to 0.96 m/s (ERA5/EGIS with grid nudging) at the ASOS site and from 2.95 m/s to 1.46 m/s on average across 28 AWS stations. Based on these results, the configuration using ERA5 reanalysis data, EGIS land-use information, and grid nudging yielded the most accurate meteorological fields and was therefore adopted for the inversion simulations. Detailed evaluation results are provided in Text S1 of the supplementary material.

For the STILT simulations, one thousand air particles were released from each observation site at the height corresponding to the measurement inlet above ground level (a.g.l.) and tracked backward in time for 24 h (Fig. 3a). A 24-hour backward period was sufficient for particles to travel beyond the innermost WRF domain (Domain 3; Fig. S2), thereby capturing the full regional influence on the observations. The STILT model was run hourly for each observation site, producing hourly footprints that represent the sensitivity of the measured CO_2 mole fraction to surface fluxes at each backward time step. The footprints were computed for an effective mixing depth below half the height of the boundary layer, considering time-varying vertical mixing depths that depend on the receptor location and meteorological conditions (Fasoli et al., 2018). The resulting footprints were vertically averaged to provide a representative surface influence field.

X-STILT extends STILT by explicitly accounting for satellite vertical profiles in the footprint calculation. For each sounding, the modelled column sensitivity was multiplied by the corresponding column-averaging kernel and pressure-weight vector to represent the XCO_2 signal. In the X-STILT simulations, one thousand air particles were released from each column level for OCO-2 and OCO-3 soundings and tracked backward for 24 h (Figs. 3b and 3c). The column receptors consisted of 37 vertical levels with 100 m spacing up to 3000 m a.g.l. and 500 m spacing up to 6000 m a.g.l. Thereafter, no particles were released above 6000 m a.g.l. to reduce computational cost, as contributions from higher altitudes to total column sensitivities are negligible. Details and equations for the footprint calculations in STILT and X-STILT are provided in Text S2 of the supplementary material.

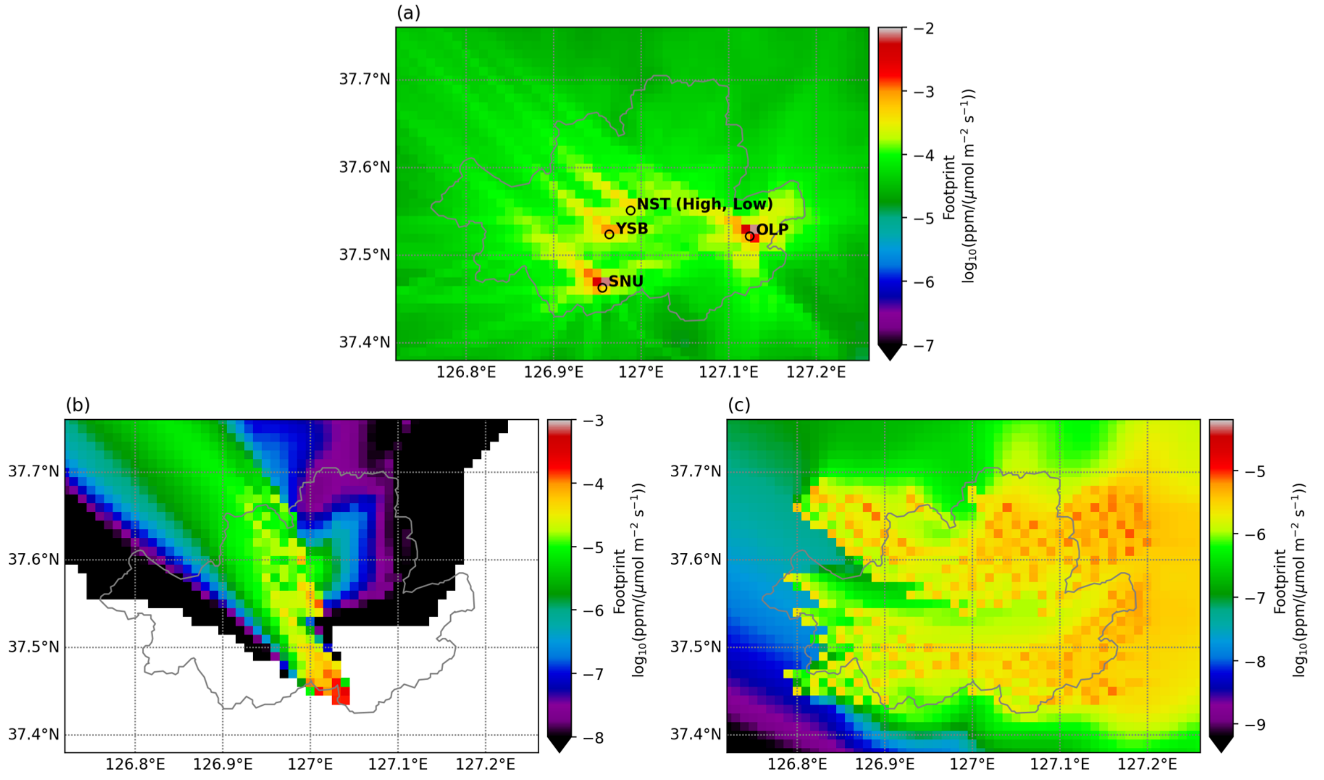

Figure 3: Footprint averages on a $\log_{10}$ scale to upwind source regions of (a) daytime-only ground observations (10:00–16:00 KST) during December 2021, (b) OCO-2 satellite data on December 4, 2021, at 13:00 KST, and (c) OCO-3 satellite data on December 5, 2021, at 11:00 KST across the Seoul domain. Note that the footprint ranges differ in panels (a), (b), and (c) for visualization purposes.

2.4 CO_2 emissions & biogenic fluxes

2.4.1 Anthropogenic CO_2 emissions

We used anthropogenic CO_2 emissions data from ODIAC version 2022 as prior emissions (Oda et al., 2018; Oda and Maksyutov, 2011). ODIAC provides global fossil fuel CO_2 emission estimates at a high spatial resolution of 1 × 1 km^2, using power plant profiles and space-based nighttime light data (Oda et al., 2018). ODIAC is based on the CDIAC national emissions estimates, which categorize emissions by fuel type—liquid, gas, solid fuel, cement, gas flare, and international bunker. The ODIAC dataset has been widely used in various research areas, such as urban emission evaluation, monitoring network design experiments, and the inverse estimation of CO_2 emissions (Che et al., 2024; Crowell et al., 2019; Fasoli et al., 2018; Hedelius et al., 2018; Kunik et al., 2019; Lauvaux et al., 2016; Lian et al., 2023, 2022; Mallia et al., 2020; Ohyama et al., 2023; Sim et al., 2023; Wu et al., 2018; Ye et al., 2020).

ODIAC is based on downscaling bottom-up CO_2 emission estimates using spatial proxies. Global geolocation information and power plant magnitudes are sourced from the Carbon Monitoring and Action database. However, this database occasionally misplaces point sources, necessitating manual correction (Kunik et al., 2019; Ohyama et al., 2023). For instance, the Korea Central Power Corporation in Seoul, located in the western part of the city, is inaccurately positioned in the ODIAC data. To correct this spatial discrepancy, we customized the ODIAC data, as shown in Fig. S3 of the supplementary material. We manually relocated the misaligned point source to match the power plant location. Additionally, for the grid cell with significantly high CO_2 emissions mistakenly identified as a point source, we replaced the emission value with the average of the surrounding eight grid cells.

Because the temporal resolution of ODIAC is monthly, it is necessary to refine the data to achieve hourly CO_2 emission estimates. We applied weekly and diurnal temporal scaling factors (Nassar et al., 2013) specific to Seoul to adjust the monthly ODIAC emission data, as shown in Fig. S4 in the supplementary material. The weekly scaling factors for Seoul remain consistent on weekdays, with values exceeding 1, but decrease over the weekends (Fig. S4a). The diurnal scaling factors exhibit typical daily emission patterns, increasing in the morning, peaking in the afternoon, and decreasing in the evening, reflecting both energy usage for heating and underlying sociodemographic activity patterns (Fig. S4b). Figure S4c shows the hourly CO_2 emissions time series after applying these temporal scaling factors. The emissions, after spatial and temporal pre-processing for December 2021, serve as the state vector for the prior CO_2 emissions, denoted as ‘$\boldsymbol{s_p}$’ (Fig. 4a).

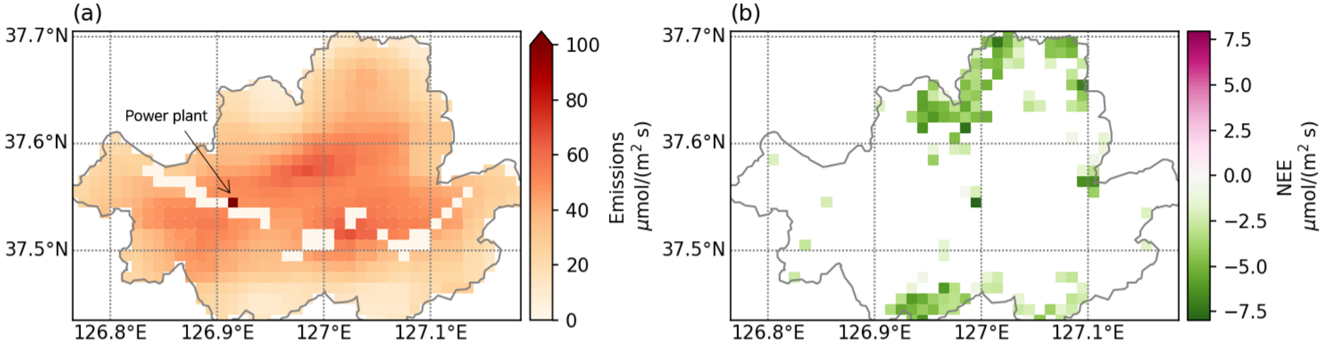

Figure 4: Averaged CO_2 fluxes of (a) prior emissions and (b) net biogenic ecosystem exchange over Seoul for daytime (10:00–16:00 KST) in December 2021. In the original ODIAC dataset, the power plant location was represented near the city center (see Fig. S3); in this study, it was corrected to its actual geographical position.

2.4.2 Biogenic CO_2 fluxes

In the urban carbon cycle, atmospheric CO_2 is mainly influenced by emissions from fossil fuel combustion and vegetation carbon uptake. Given that Seoul has forests covering 25.3% of its total area (Korea Forest Service, 2021), the impact of biogenic CO_2 fluxes cannot be ignored. To account for the influence of biogenic CO_2 on the observed concentration, we incorporated biogenic CO_2 fluxes estimated by a data-based model known as CASS (Carbon Simulator from Space). CASS generates terrestrial carbon flux data from vegetation using information such as air temperature, relative humidity, photosynthetically active radiation, enhanced vegetation index, and land surface water index. CASS employs the random forest method to determine optimal coefficients for each region and applies them to the estimation of carbon uptake. We utilized hourly net ecosystem exchange (NEE) data, which were resampled from a 250-meter resolution to 0.01°, as the biogenic CO_2 flux data within Seoul (Fig. 4b). CO_2 uptake can be observed in grids where Seoul's mountains and parks are located during the daytime. We obtained the vegetation-affected concentration by multiplying the footprints from the atmospheric transport model by the gridded biogenic CO_2 flux data using Eq. (S2) or (S4).

2.5 Prior error covariance

The prior error covariance matrix ($\boldsymbol{Q}$) is derived from both the variance in prior emissions uncertainty ($\boldsymbol{\sigma}$) and the temporal and spatial covariances ($\boldsymbol{D}$ and $\boldsymbol{E}$). We construct the prior error covariance matrix as follows:

$$\boldsymbol{Q} = \boldsymbol{I_\sigma}(\boldsymbol{D} \otimes \boldsymbol{E})\boldsymbol{I_\sigma} \tag{6}$$

Where $\boldsymbol{I_\sigma}$ is a diagonal matrix whose elements represent the uncertainty of prior emissions. Instead of directly constructing the full $\boldsymbol{Q}$ matrix, the temporal and spatial error covariance matrices are combined using a Kronecker product ($\otimes$) to reduce computational costs, particularly when dealing with large emission state vectors (Yadav and Michalak, 2013).

In previous studies on urban inverse modelling, three methods for estimating prior emissions uncertainty were mainly identified. Most studies assumed a relative uncertainty for prior estimates, such as 30% uncertainty for each emission source in Central California (Zhao et al., 2009), 15% for large point sources and 85% for the rest in Tokyo (Ohyama et al., 2023), 20% for Los Angeles and 40% for Riyadh and Cairo (Ye et al., 2020), 20% (Lian et al., 2022), and 60% (Nalini et al., 2022) for Paris. Kunik et al. (2019) and Mallia et al. (2020) defined the uncertainty of prior emissions as the difference between the prior and true emission estimates (e.g., Hestia). Another approach to estimating prior emissions uncertainty is inter-comparison with different inventories (Sargent et al., 2018; Wu et al., 2018). In this study, we assumed a relative uncertainty of 15% for large point sources and 100% for the rest of Seoul, similar to the approach used for Tokyo in Ohyama et al. (2023). For grids with prior emissions of 0 μmol m^{-2} s^{-1}, such as rivers, a minimum uncertainty value of 1 μmol m^{-2} s^{-1} was assigned, following the method of Kunik et al. (2019).

The temporal and spatial covariance matrices are defined using exponential decay equations:

$$\boldsymbol{D} = \exp\left(-\frac{X_\tau}{l_\tau}\right) \tag{7}$$

$$\boldsymbol{E} = \exp\left(-\frac{X_s}{l_s}\right) \tag{8}$$

The temporal covariance is computed based on lag-times ($\boldsymbol{X_\tau}$) between time steps, divided by temporal correlation range parameters ($\boldsymbol{l_\tau}$), where $\boldsymbol{l_\tau}$ represents the time over which the correlation decays significantly. Similarly, the spatial covariance is calculated using separation distances ($\boldsymbol{X_s}$) between grid cells, divided by spatial correlation range parameters ($\boldsymbol{l_s}$), where $\boldsymbol{l_s}$ indicates the distance over which the correlation decays significantly. Previous studies have shown that suitable spatiotemporal correlation parameters vary by city. For example, in Salt Lake City, the temporal and spatial correlations were determined to be 2 d and 6 km, respectively (Kunik et al., 2019), whereas in Tokyo, the parameters were 0 d and 10 km (Ohyama et al., 2023). We performed a lagged autocorrelation function and variogram analysis to determine the optimal temporal and spatial correlation lengths for Seoul, respectively (Fig. S5). Based on the results, the optimal temporal and spatial correlation range parameters for the inversion over Seoul were 9 h and 10 km, respectively.

2.6 Observational error covariance

We estimated the observational error covariance ($\boldsymbol{R}$) using the departure-based diagnostics, commonly known as the Hollingsworth/Lönnberg method (Hollingsworth and Lönnberg, 1986; Lönnberg and Hollingsworth, 1986; Rutherford, 1972). The departure (or innovation) is defined as $\boldsymbol{z} - \boldsymbol{Hs_p}$, representing the difference between the observed $\triangle CO_2$ and the values simulated by WRF-(X)STILT with prior emissions, following Eqs. (S2) and (S4). Because the standard deviation of departures reflects the combined effects of observation and prior emissions errors, we separate their contributions based on certain assumptions. The Hollingsworth/Lönnberg method assumes that prior emissions errors exhibit spatial correlation, whereas observation errors are spatially uncorrelated (Bormann et al., 2009). Additionally, prior emissions and observation errors are considered independent. Here, observation error includes uncertainties arising from the instrument, transport model, representation, background inflow (boundary conditions), and biogenic fluxes.

To estimate observation errors, we first compute the covariance of departure pairs as a function of separation distance. A function is then fitted to the covariance values at various distances, excluding the value at zero separation, and extrapolated to estimate the covariance at zero distance. At zero separation, the total variance is decomposed into a spatially correlated component (representing prior emissions error) and an uncorrelated component (representing observation error). Based on these assumptions, the value of the fit gives the prior emissions error in observation space at zero separation, and the observation error is determined by subtracting this value from the total covariance at zero distance.

In this study, we applied the Hollingsworth/Lönnberg method to estimate the observational error covariance for both ground-based and satellite observations. We first divided the observation vector into subsets: NST_H, NST_L, OLP, SNU, YSB, OCO-2, and OCO-3, assuming that error statistics within each subset are homogeneous. Because this method was originally developed for satellite data, which has wide spatial coverage but infrequent revisit cycles, we applied it directly for satellite observations. We assumed satellite observation errors are spatially uncorrelated and fitted a function (Limited-memory Broyden-Fletcher-Goldfarb-Shanno with Box constraints in R language) to the covariance as a function of separation distance. For ground-based observations, which provide data over a long period, we assumed that observation errors are temporally uncorrelated. Instead of using spatial distance, we fitted a function to the covariance as a function of time steps. The inferred observation error for each dataset was obtained by subtracting the value of the fit at zero separation (distance or time step) from the total covariance. The fitting results for each observation type are shown in Fig. S6. The inferred observation error was multiplied by the square of the standard deviation of departures, and the square of the mean departure was added to correct for bias. Finally, the estimated observation error for each observation was placed on the diagonal of the R matrix.

3 Results and discussion

In Sect. 3.1, we compare CO_2 emissions from prior and posterior estimates to investigate the spatiotemporal differences following the inversion run. In Sect. 3.2, we assess CO_2 enhancement between observations and simulations using prior and posterior emissions to evaluate the effectiveness of the inversion. In Sect. 3.3, we conducted a series of sensitivity analyses to evaluate the robustness of the inversion results. First, we examined the constraint effects by performing sensitivity tests using all observations, only ground-based data, only OCO-2 data, and only OCO-3 data, along with UR analysis. Additionally, we investigated how the assumptions in the inverse modelling framework affect the inversion outcomes by varying the treatment of background concentrations for ground-based and satellite observations, biogenic fluxes, and the relative uncertainties assigned to prior emissions. A comprehensive discussion accompanies each set of results.

3.1 Comparison between prior and posterior emissions

We obtained posterior CO_2 emissions over Seoul for December 2021 using Bayesian inverse modelling, incorporating ground-based and satellite observations. Figure 5a compares the average CO_2 emissions between the prior and posterior estimates. The mean daytime prior and posterior emissions were 34.12 and 35.63 μmol m^{-2} s^{-1}, corresponding to approximately 2.43 and 2.54 million metric tons of CO_2 for December 2021 over Seoul, respectively. The average correction from prior to posterior emissions was approximately +4.43%, suggesting a slight increase in posterior emissions, and the prior emissions were slightly underestimated. However, the difference between the domain- and time-averaged prior and posterior emissions was not statistically significant. Similar findings have been reported in previous studies conducted in Tokyo (Ohyama et al., 2023). The reduced chi-squared value for the posterior emissions was 1.38. Although this is slightly higher than the ideal value of 1.0, it still indicates a reasonable representation of prior emissions error and observation error covariance assumptions. Further reducing this value closer to 1 would require assuming larger error metrics.

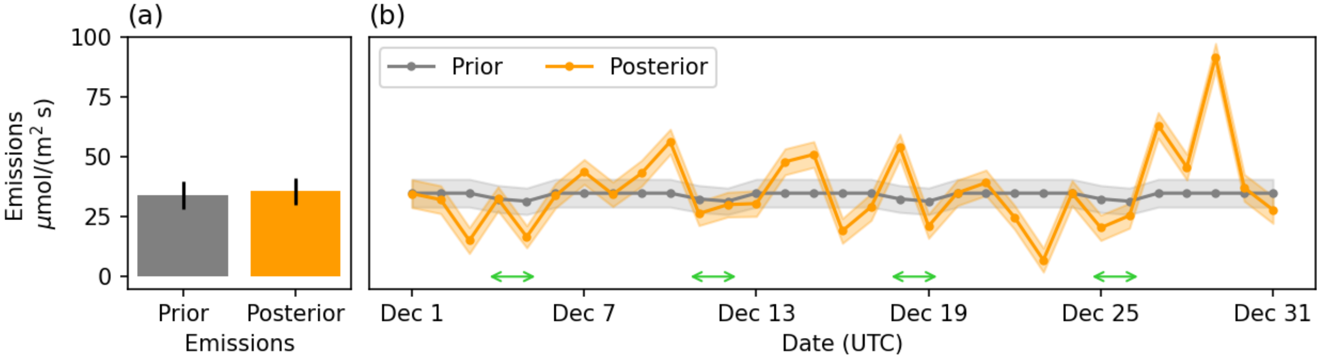

Figure 5: (a) Comparison of time- and domain-averaged emissions between prior and posterior estimates for December 2021 in Seoul, and (b) time series of domain-averaged daily (daytime average) prior and posterior CO_2 emissions, including emission uncertainties. Green arrows indicate weekends.

The daily time series of temporally resolved prior and posterior emissions averaged over the Seoul domain is shown in Fig. 5b. The prior emissions show relatively low temporal variability, with a standard deviation of 1.28 μmol m^{-2} s^{-1} and a range from 31.5 to 34.86 μmol m^{-2} s^{-1}. In contrast, the posterior emissions exhibit substantially greater temporal variability (standard deviation = 16.18 μmol m^{-2} s^{-1}, range: 6.95–91.73 μmol m^{-2} s^{-1}), capturing realistic fluctuations driven by diverse sources such as traffic, building heating, manufacturing, and energy production. For the prior emissions, the monthly ODIAC data was pre-processed using temporal scaling factors, resulting in slightly higher emissions on weekdays and lower emissions on weekends. The posterior time series did not show a clear distinction between weekday and weekend patterns; however, the average emissions were 38.16 and 28.36 for weekdays and weekends, respectively, with weekday emissions being 1.35 times higher than those on weekends. Posterior emissions fluctuated throughout the month, with a sharp increase from December 27 to 29, reaching values close to two standard deviations above the monthly mean. This rise may associated with higher heating demand due to lower temperatures and a rebound in traffic activity following the holiday.

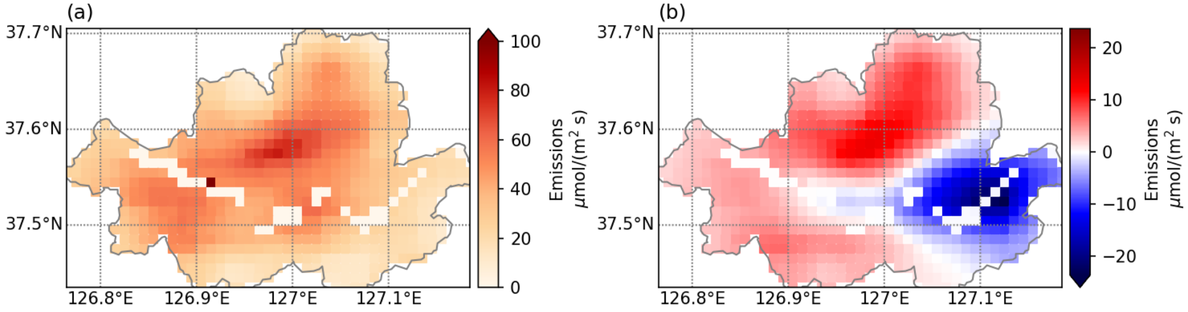

Figure 6: Averaged CO_2 fluxes over Seoul for daytime over December 2021. (a) Posterior emissions and (b) emission corrections (posterior minus prior) after the inversion run that used five ground sites, OCO-2, and OCO-3 data.

Figure 6 shows the spatial distribution of posterior CO_2 emissions and emission corrections from the inversion using all observation data over Seoul. Compared to the spatial patterns of prior CO_2 emissions in Fig. 4a, the posterior emissions in Fig. 6a exhibit a similar distribution, with higher emissions concentrated in central Seoul and lower emissions near the city's boundaries. However, the posterior correction map, obtained by subtracting prior emissions from posterior emissions, reveals spatial variations in emission adjustments ranging from −23.59 to 13.61 μmol m^{-2} s^{-1} (Fig. 6b). Most areas in Seoul experienced either increased or decreased emissions through Bayesian inverse modelling. Notably, emissions in the eastern part of Seoul were strongly corrected in the negative direction, whereas most other regions underwent positive corrections. This suggests that prior emissions were overestimated in the eastern part of Seoul and underestimated in the other areas. The eastern part of Seoul, including Songpa District, is dominated by residential areas with lower traffic and industrial activity compared to central Seoul. As ODIAC's spatial allocation relies on nighttime light intensity, which can be misleadingly high in residential zones, prior emissions were likely overestimated, resulting in negative corrections in the posterior estimates. In contrast, the central part of Seoul, particularly Jung-gu, exhibited strong positive corrections in the posterior emissions. This area represents the city's main commercial and business district, characterized by dense traffic networks, high daytime population, and substantial building energy use. As noted by Oda et al. (2018, 2019), ODIAC's spatial disaggregation method does not fully capture emissions from line sources such as the transport sector, which can lead to underestimation in areas with heavy road traffic. Consequently, the posterior optimization increased emissions in Jung-gu to better match the observed concentrations, correcting for the limitations of the prior inventory.

3.2 Comparison of CO_2 enhancement between observation and simulation

A comparison between observed CO_2 enhancements (OBS) and simulated CO_2 enhancements (MOD) was conducted to evaluate the performance of the inversion framework and assess how well atmospheric CO_2 data constrained emissions over Seoul. Figure 7 shows the changes in the relationship between OBS and MOD from prior to posterior emissions. MOD, based on prior emissions, was significantly lower than OBS, with a slope of 0.39 in Fig. 7a. However, after the inversion, the discrepancies were reduced, and MOD became closer to OBS, with the slope increasing to 0.71. The posterior slope does not reach 1 because the inversion balances uncertainties from both the observations and the prior emissions. Although observational errors are typically smaller than prior emission uncertainties, which brings the posterior MOD closer to OBS, the constraints applied to the prior prevent the posterior slope from fully reaching 1. The correlation coefficient between OBS and MOD improved from 0.46 to 0.85, indicating a better agreement after the inversion.

The MAE between OBS and MOD also decreased significantly, from 12.18 to 6.64 ppm, when using posterior emissions data, shown in Fig. 7b. The MAE between observed and modelled ΔCO_2 from posterior emissions for the different background configurations were 6.84, 6.64, and 7.20 ppm for GM1, GM2, and GM3, respectively, and 6.76, 6.64, and 6.65 ppm for SM1, SM2, and SM3, confirming that GM2 and SM2 provided the best agreement with the observations. These results indicate that the inversion framework effectively constrained CO_2 emissions over Seoul by incorporating information from observational data.

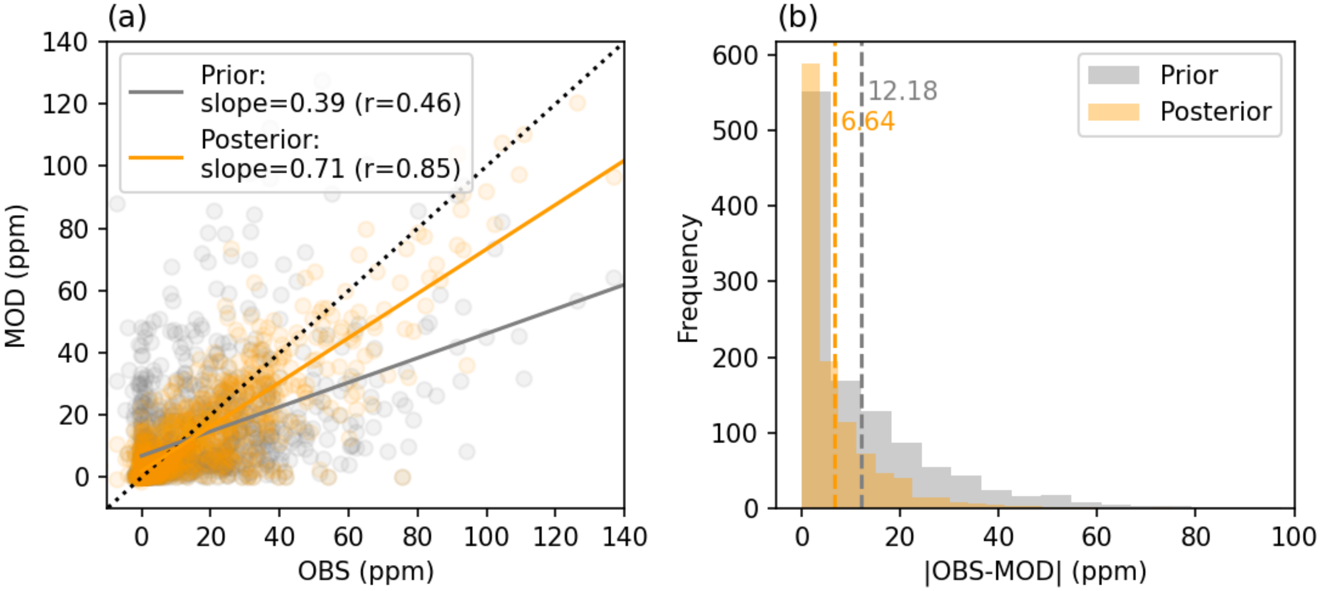

Figure 7: Comparison of observed CO_2 enhancements (OBS) and simulated CO_2 enhancements (MOD) using prior (gray) and posterior (orange) emissions during daytime over December 2021. (a) Scatter plots of OBS vs. MOD, with the slope and correlation coefficient (r). (b) Frequency distributions of absolute differences between OBS and MOD (|OBS-MOD|). The dashed lines in (b) indicate the average MAE between OBS and MOD.

3.3 Sensitivity test

3.3.1 Observational network

We evaluated the performance of the inverse model through a sensitivity analysis considering different observational network configurations (Fig. 8). The cases included 1) using all observation data, 2) using only five ground sites, 3) using only OCO-2 data, and 4) using only OCO-3 data. The most substantial reductions in uncertainty were observed when all available observations were used, with an average reduction exceeding 19.2% (Fig. 8a). In this case, the spatial distribution of UR was similar to that obtained using only ground sites (Fig. 8b), as ground-based observations had a greater influence on the constraint than satellite data because of their continuous temporal coverage throughout the entire month. The spatial difference in UR between using all observations and using only the five ground sites is shown in Figure S7. When using five ground sites, the UR in posterior emissions was 18.7%. The largest reductions occurred where ground observation sites were concentrated, particularly around OLP (eastern region), SNU (southern region), and surrounding $\mathrm{NST_H}$, $\mathrm{NST_L}$, and YSB. The reduction in uncertainty extended beyond the observation sites, covering the broader footprint influence range in Fig. 3a. Notably, a decrease was observed northwest of the observation sites, the upwind region. However, the impact on UR was minimal in western and northern Seoul, where no ground-based observation sites were present.

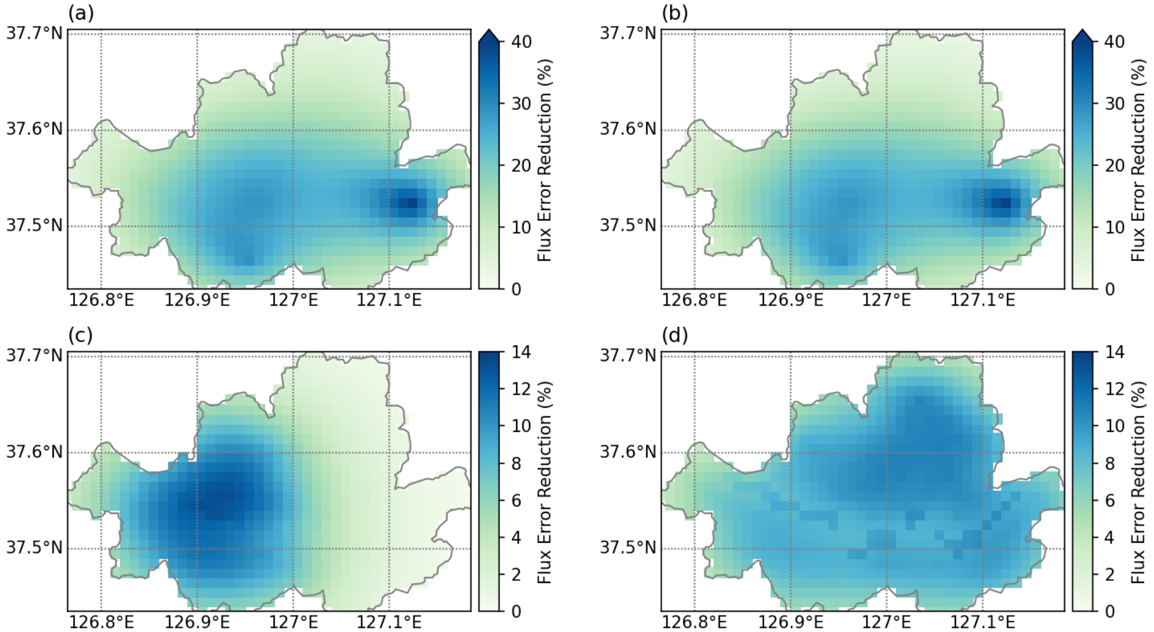

Figure 8: Daytime percent UR in posterior emissions over Seoul for the inverse analysis using different observation datasets: (a) all observation data from December 2021, (b) only five ground sites from December 2021, (c) only OCO-2 data from December 3–5,

2021, and (d) only OCO-3 data from December 3–5, 2021, when the satellite passed over Seoul. Note that the percent reduction ranges in panels (a), (b), (c), and (d) vary for visualization purposes.

Because OCO-2 and OCO-3 passed over Seoul on December 4 and 5, 2021, respectively, the UR results for satellite data are focused on December 3–5, highlighting the effect of satellite observations. The OCO-2 data significantly reduced the uncertainty of posterior emissions over western Seoul, with an average reduction of 6% (Fig. 8c). This can be attributed to the satellite's north-to-south overpass, covering the western footprint, an upwind region in Fig. 3b. OCO-2 contributed to UR in the western parts of Seoul, areas not covered by ground-based observations. Most of Seoul experienced UR due to OCO-3, which had 167 soundings across the city (Fig. 8d). The domain-averaged UR from December 3–5 was 8.4%. OCO-3 contributed to UR in the northern region of Seoul, which was not covered by ground-based or OCO-2 observations. The extensive coverage of satellite observations enabled further corrections in areas lacking ground observations, demonstrating the added value of satellite constraints in reducing uncertainty.

The impacts of different observational datasets on the posterior emission estimates are summarized in Fig. S8. Satellite observations influenced the inversion only on the days when OCO-2 or OCO-3 overpassed Seoul, with corrections primarily occurring around December 3–5. Specifically, on December 3–4, satellite-based corrections increased emissions while ground-based observations tended to reduce them, reflecting opposing influences. These differences highlight that the spatial and temporal coverage of observations can lead to distinct patterns of emission corrections across the inversion domain. On December 5, OCO-3 and ground-based data contributed to decreased emissions with nearly consistent magnitudes.

3.3.2 Model inputs and assumptions

To evaluate how the assumptions made for components of the inverse modelling framework affect the inversion results, we conducted a series of sensitivity analyses considering background concentrations for ground-based and satellite observations, biogenic fluxes, and the relative uncertainty assigned to prior emissions (Fig. 9). The sensitivity experiments were performed based on a reference configuration, which used the GM2 method for ground-based background estimation, the SM2 method for satellite-based background estimation, included biogenic fluxes, and assumed a 100 % relative uncertainty for prior emissions. Each sensitivity experiment altered only one variable at a time while keeping the others fixed at the reference configuration.

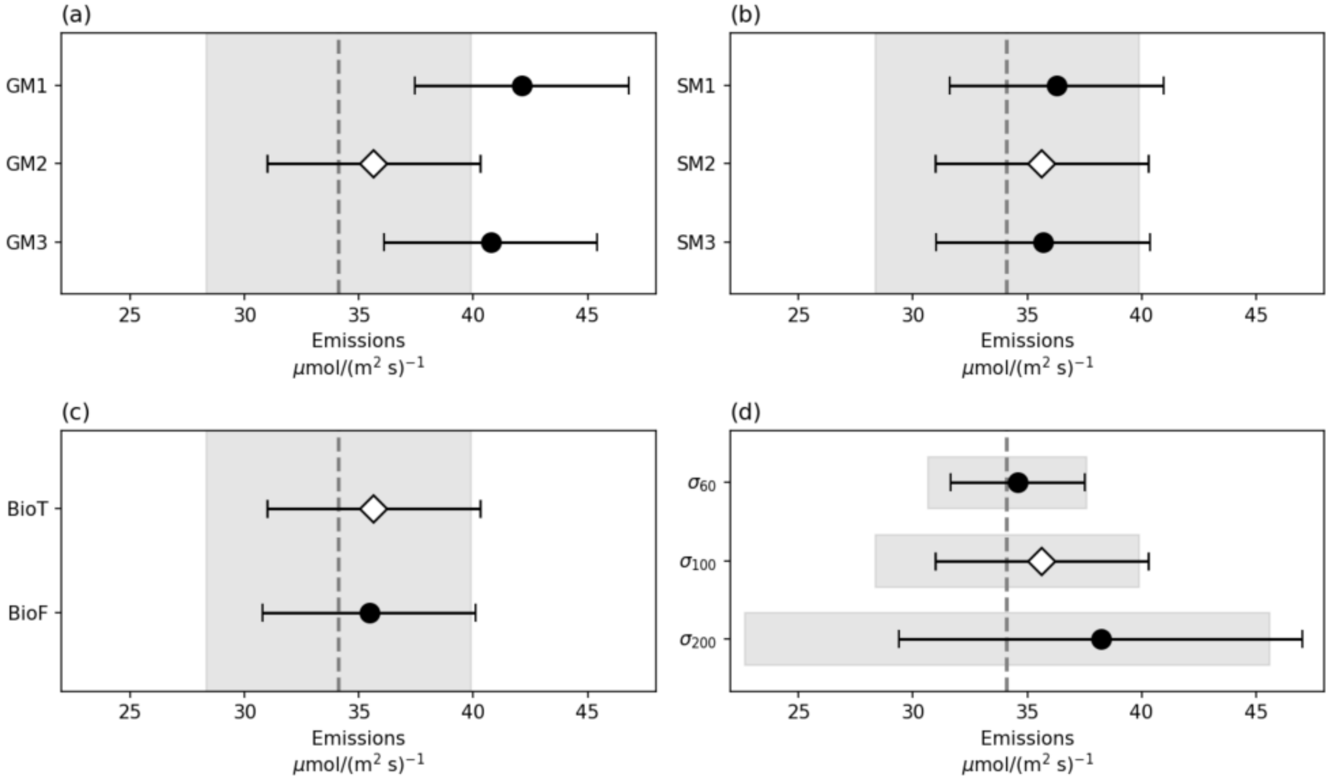

Figure 9: Sensitivity tests showing changes in posterior CO_2 emissions for (a) ground-based observation background, (b) satellite observation background, (c) with and without biogenic flux, and (d) the relative uncertainty of prior emissions for December 2021 in Seoul. The vertical dashed line and shaded area represent the averaged prior CO_2 emissions and their uncertainty range, respectively. The diamond symbols denote the posterior emissions derived from the reference inverse analysis, while the filled circles indicate the results from sensitivity experiments.

Regardless of the assumptions, the CO_2 emissions increased after the inversion in all experiments. In the ground-based background experiment, the degree of increase in posterior emissions varied substantially depending on the background estimation method (Fig. 9a). When the GM2 method (reference) was used, the posterior emissions increased by 4.43% compared with the prior emissions, while the GM1 and GM3 methods resulted in increases of 23.48% and 19.47%, respectively. This large difference arises from the substantial variation in the background CO_2 levels among methods. The mean background concentrations averaged over all ground sites were 443.45 ppm for GM2, whereas GM1 and GM3 produced much lower averages of 436.01 ppm and 437.98 ppm, respectively. Consequently, the derived ΔCO_2 values were larger for GM1 and GM3. During periods when GM2 adjusted the emissions upward, GM1 and GM3 also increased their estimates but to a much larger extent, resulting in substantial overestimation (Fig. S9). Although GM2 was selected as the reference configuration because it yielded the smallest MAE between the posterior-modelled and observed enhancements, the large variation in posterior emission magnitudes across background estimation methods highlights the critical importance of selecting an appropriate background representation for urban inversions.

For the satellite-based background experiment, the differences among background estimation methods were smaller than those for the ground-based cases (Fig. 9b). Starting from a prior mean of 34.119 μmol m^{-2} s^{-1}, the posterior means obtained using SM1, SM2, and SM3 were 36.282, 35.631, and 35.689, respectively. This is because the estimated background concentrations were relatively consistent across the SM1, SM2, and SM3 methods—417.69, 418.63, and 418.24 ppm for OCO-2 and 417.48, 418.64, and 418.72 ppm for OCO-3, respectively. Because satellite CO_2 concentrations are generally lower than ground-based values, the resulting ΔCO_2 is more sensitive to background assumptions. In addition, each satellite observation represents a wide spatial area, giving it relatively strong leverage in the inversion. Consequently, any differences in the assumed satellite background concentrations for Seoul would have led to correspondingly larger changes in the inferred emissions.

Including biogenic fluxes slightly increased the posterior emissions by 0.17 μmol m^{-2} s^{-1} compared with the case without biogenic fluxes (Fig. 9c). The higher posterior emissions when biogenic fluxes were included can be attributed to daytime photosynthetic CO_2 uptake by vegetation. If the observed CO_2 concentrations are affected by this uptake, they represent an atmosphere that has already been partially depleted of CO_2. Thus, the measured concentrations imply greater fossil-fuel emissions to produce the same observed levels. The resulting increase in ΔCO_2 causes the inversion to adjust emissions upward. However, the overall effect was small, likely because the study period (December) corresponds to the dormant season with limited biogenic activity.

Finally, the sensitivity experiment on the relative uncertainty of prior emissions showed that larger prior uncertainties led to stronger emission adjustments (Fig. 9d). As the relative uncertainty increases, the prior emission covariance matrix becomes larger, effectively giving greater weight to the observational constraints during inversion. The UR were 15.5%, 19.2%, and 23.2% for relative uncertainties of 60%, 100%, and 200%, respectively. These results demonstrate that the selection of appropriate uncertainty values for prior emissions is crucial in determining both the magnitude of posterior emissions and the UR in urban-scale inverse modelling.

4 Summary and conclusions

This study developed a Bayesian inverse modelling framework (version 1) to optimize CO_2 emissions using both ground- and space-based observations and applied it to Seoul. By incorporating high-resolution (0.01° spatial, 1 h temporal) anthropogenic and biogenic CO_2 fluxes, atmospheric CO_2 measurements, a Lagrangian transport model, and uncertainty quantification, we improved the accuracy of emission estimates. For Seoul, ground-based (NST_H, NST_L, OLP, SNU, YSB) and satellite (OCO-2, OCO-3) observations from December 2021 were used to constrain emissions, with WRF-(X)STILT footprints linking emissions to observed CO_2 enhancements.

Integrating ground- and satellite-based observations revealed substantial spatiotemporal variations. Posterior emissions exhibited greater variability, capturing both underestimation in most areas and overestimation in eastern Seoul. This combined observational approach not only improved overall emission estimates but also provided detailed insights into spatial and temporal patterns at fine scales, which are critical for tracking when and where CO_2 emissions fluctuate and assess the impact of carbon reduction policies over time and space. The inversion highlighted periods of substantial emission increases and identified areas of under- and overestimation, providing information to improve bottom-up emission inventories and offering important policy implications for urban climate action and emissions mitigation. Comparing observed and simulated CO_2 enhancements confirmed the effectiveness of the inversion, reducing the MAE by nearly half. Sensitivity tests showed that ground- and space-based data achieved the greatest UR (19.2%), with OCO-2 and OCO-3 providing critical constraints in areas lacking ground-based observations. These results emphasize the complementary role of satellite data, particularly OCO-3's snapshot capability, in enhancing urban CO_2 monitoring. We also revealed that assumptions regarding background concentrations, biogenic fluxes, and prior emission uncertainties can meaningfully influence posterior emissions, underscoring the importance of carefully evaluating model inputs.

Despite these improvements, some limitations remain, which future work will address. First, the inversion results depend on the accuracy of the transport model, introducing uncertainties in simulating atmospheric transport. Comparison with observed wind speeds indicates that the model slightly overestimates wind, which could lead to a modest underestimation of posterior CO_2 emissions by enhancing simulated transport and dilution. Future improvements to WRF-(X)STILT will aim to reduce discrepancies between modelled and observed meteorological fields through enhanced terrain elevation data and observation nudging. And this study relied solely on daytime observations, and therefore the influence of CO_2 concentrations associated with other periods, such as morning and evening rush-hour emissions, was not reflected in the inversion results. Future work will focus on improving the model representation of the nocturnal planetary boundary layer to enable the use of the full diurnal cycle of observations, which would provide better constraints on CO_2 emissions. Second, the analysis focused on a 1-month period, which was intentionally selected to evaluate the initial performance of the inversion framework (v1) and to identify areas for improvement. We selected 2021 as it was the first year with complete CO_2 measurements from all ground-based sites in Seoul. December was chosen because biogenic influences are minimal and both OCO-2 and OCO-3 passed over Seoul during this month, enabling consistent integration of ground-based and satellite observations. In future work, the inversion system will be extended to longer temporal periods to capture seasonal variations in emissions and to enable more comprehensive evaluation of the results through comparisons with Korea's national greenhouse gas inventory and previous studies. Third, although the reduced chi-square value has been evaluated, additional validation using independent datasets such as radiocarbon ($\Delta^{14}C$) and flux tower measurements will be conducted.

This approach can be applied to other cities, enabling an independent evaluation of city-reported emissions and identifying discrepancies between reported and observation-constrained estimates. By diagnosing the causes of these differences and progressively reducing them, more robust and transparent emission estimates can be achieved, providing valuable insights for urban mitigation planning and supporting the development of evidence-based climate policies.

Data Availability

The prior emissions data from ODIAC were obtained from the Center for Global Environmental Research (https://www.odiac.org/data-product.html). Biogenic CO_2 fluxes data from the CASS were downloaded from the Korea Carbon Project website (https://korea-carbon-project.org/map). The WRF model is freely distributed to the scientific community by the National Center for Atmospheric Research (NCAR) and can be accessed at https://www2.mmm.ucar.edu/wrf/users/download/get_source.html. The STILT and X-STILT models available for installation at https://uataq.github.io/stilt/#/ and https://github.com/uataq/X-STILT, respectively. CO_2 measurements from the five ground observation sites used in this study are available upon request from the corresponding author. OCO-2 and OCO-3 satellite data are publicly available from https://ocov2.jpl.nasa.gov/science/oco-2-data-center/ and https://ocov3.jpl.nasa.gov/science/oco-3-data-center/, respectively.

Competing interests

The authors declare that they have no conflict of interest.

Acknowledgments

This work was supported by Korea Environmental Industry & Technology Institute (KEITI) through "Project for developing an observation-based GHG emissions geospatial information map", funded by Korea Ministry of Environment (MOE) (RS-2023-00232066).

References

Ahn, D. Y., Goldberg, D. L., Coombes, T., Kleiman, G., and Anenberg, S. C.: CO2 emissions from C40 cities: citywide emission inventories and comparisons with global gridded emission datasets, Environ. Res. Lett., 18, https://doi.org/10.1088/1748-9326/acbb91, 2023.

Ammoura, L., Xueref-Remy, I., Gros, V., Baudic, A., Bonsang, B., Petit, J. E., Perrussel, O., Bonnaire, N., Sciare, J., and Chevallier, F.: Atmospheric measurements of ratios between CO2 and co-emitted species from traffic: a tunnel study in the Paris megacity, Atmos. Chem. Phys., 14, 12871–12882, https://doi.org/10.5194/acp-14-12871-2014, 2014.

Bares, R., Lin, J. C., Hoch, S. W., Baasandorj, M., Mendoza, D. L., Fasoli, B., Mitchell, L., Catharine, D., and Stephens, B. B.: The wintertime covariation of CO2 and criteria pollutants in an urban valley of the Western United States, J. Geophys. Res. Atmos., 123, 2684–2703, https://doi.org/10.1002/2017JD027917, 2018.

Bormann, N., Collard, A., and Bauer, P.: Estimates of spatial and inter-channel observation error characteristics for current sounder radiances for NWP, ECMWF Tech. Memo., 1–41, https://doi.org/10.21957/l9qde2741, 2009.

Breón, F. M., Broquet, G., Puygrenier, V., Chevallier, F., Xueref-Remy, I., Ramonet, M., Dieudonné, E., Lopez, M., Schmidt, M., Perrussel, O., and Ciais, P.: An attempt at estimating Paris area CO2 emissions from atmospheric concentration measurements, Atmos. Chem. Phys., 15, 1707–1724, https://doi.org/10.5194/acp-15-1707-2015, 2015.

Chandra, N., Lal, S., Venkataramani, S., Patra, P. K., and Sheel, V.: Temporal variations of atmospheric CO2 and CO at Ahmedabad in western India, Atmos. Chem. Phys., 16, 6153–6173, https://doi.org/10.5194/acp-16-6153-2016, 2016.

C40 Cities: C40 Annual Report 2022, C40 Cities, https://www.c40.org/about-c40/#annualreport, 2022.

Che, K., Lauvaux, T., Taquet, N., Stremme, W., Xu, Y., Alberti, C., Lopez, M., García-Reynoso, A., Ciais, P., Liu, Y., Ramonet, M., and Grutter, M.: CO2 Emissions Estimate From Mexico City Using Ground- and Space-Based Remote Sensing, J. Geophys. Res. Atmos., 129, https://doi.org/10.1029/2024JD041297, 2024.

Crowell, S., Baker, D., Schuh, A., Basu, S., Jacobson, A. R., Chevallier, F., Liu, J., Deng, F., Feng, L., McKain, K., Chatterjee, A., Miller, J. B., Stephens, B. B., Eldering, A., Crisp, D., Schimel, D., Nassar, R., O'Dell, C. W., Oda, T., Sweeney, C., Palmer, P. I., and Jones, D. B. A.: The 2015–2016 carbon cycle as seen from OCO-2 and the global in situ network, Atmos. Chem. Phys., 19, 9797–9831, https://doi.org/10.5194/acp-19-9797-2019, 2019.

Enting, I. G.: Inverse Problems in Atmospheric Constituent Transport, Cambridge University Press, 2002.

Fasoli, B., Lin, J. C., Bowling, D. R., Mitchell, L., and Mendoza, D.: Simulating atmospheric tracer concentrations for spatially distributed receptors: Updates to the Stochastic Time-Inverted Lagrangian Transport model's R interface (STILT-R version 2), Geosci. Model Dev., 11, 2813–2824, https://doi.org/10.5194/gmd-11-2813-2018, 2018.

Feng, S., Lauvaux, T., Newman, S., Rao, P., Ahmadov, R., Deng, A., Díaz-Isaac, L. I., Duren, R. M., Fischer, M. L., Gerbig, C., Gurney, K. R., Huang, J., Jeong, S., Li, Z., Miller, C. E., O'Keeffe, D., Patarasuk, R., Sander, S. P., Song, Y., Wong, K. W., and Yung, Y. L.: Los Angeles megacity: A high-resolution land-atmosphere modelling system for urban CO2 emissions, Atmos. Chem. Phys., 16, 9019–9045, https://doi.org/10.5194/acp-16-9019-2016, 2016.

Friedlingstein, P., O’sullivan, M., Jones, M. W., Andrew, R. M., Gregor, L., Hauck, J., Le Quéré, C., Luijkx, I. T., Olsen, A., Peters, G. P., Peters, W., Pongratz, J., Schwingshackl, C., Sitch, S., Canadell, J. G., Ciais, P., Jackson, R. B., Alin, S. R., Alkama, R., Arneth, A., Arora, V. K., Bates, N. R., Becker, M., Bellouin, N., Bittig, H. C., Bopp, L., Chevallier, F., Chini, L. P., Cronin, M., Evans, W., Falk, S., Feely, R. A., Gasser, T., Gehlen, M., Gkritzalis, T., Gloege, L., Grassi, G., Gruber, N., Gürses, Ö., Harris, I., Hefner, M., Houghton, R. A., Hurtt, G. C., Iida, Y., Ilyina, T., Jain, A. K., Jersild, A., Kadono, K., Kato, E., Kennedy, D., Klein Goldewijk, K., Knauer, J., Korsbakken, J. I., Landschützer, P., Lefèvre, N., Lindsay, K., Liu, J., Liu, Z., Marland, G., Mayot, N., Mcgrath, M. J., Metzl, N., Monacci, N. M., Munro, D. R., Nakaoka, S. I., Niwa, Y., O’brien, K., Ono, T., Palmer, P. I., Pan, N., Pierrot, D., Pocock, K., Poulter, B., Resplandy, L., Robertson, E., Rödenbeck, C., Rodriguez, C., Rosan, T. M., Schwinger, J., Séférian, R., Shutler, J. D., Skjelvan, I., Steinhoff, T., Sun, Q., Sutton, A. J., Sweeney, C., Takao, S., Tanhua, T., Tans, P. P., Tian, X., Tian, H., Tilbrook, B., Tsujino, H., Tubiello, F., Van Der Werf, G. R., Walker, A. P., Wanninkhof, R., Whitehead, C., Willstrand Wranne, A., et al.: Global Carbon Budget 2022, Earth Syst. Sci. Data, 14, 4811–4900, https://doi.org/10.5194/essd-14-4811-2022, 2022.

Gamage, L. P., Hix, E. G., and Gichuhi, W. K.: Ground-Based Atmospheric Measurements of CO:CO2 Ratios in Eastern Highland Rim Using a CO Tracer Technique, ACS Earth Space Chem., 4, 558–571, https://doi.org/10.1021/acsearthspacechem.9b00322, 2020.

Gately, C. K., Hutyra, L. R., and Wing, I. S.: Cities, traffic, and CO2: A multidecadal assessment of trends, drivers, and scaling relationships, Proc. Natl. Acad. Sci. U. S. A., 112, 4999–5004, https://doi.org/10.1073/pnas.1421723112, 2015.

Göckede, M., Turner, D. P., Michalak, A. M., Vickers, D., and Law, B. E.: Sensitivity of a subregional scale atmospheric inverse CO2 modeling framework to boundary conditions, J. Geophys. Res. Atmos., 115, https://doi.org/10.1029/2010JD014443, 2010.

Gurney, K. R., Razlivanov, I., Song, Y., Zhou, Y., Benes, B., and Abdul-Massih, M.: Quantification of fossil fuel CO2 emissions on the building/street scale for a large U.S. City, Environ. Sci. Technol., 46, 12194–12202, https://doi.org/10.1021/es3011282, 2012.

Gurney, K. R., Liang, J., O’Keeffe, D., Patarasuk, R., Hutchins, M., Huang, J., Rao, P., and Song, Y.: Comparison of Global Downscaled Versus Bottom-Up Fossil Fuel CO2 Emissions at the Urban Scale in Four U.S. Urban Areas, J. Geophys. Res. Atmos., 124, 2823–2840, https://doi.org/10.1029/2018JD028859, 2019a.

Gurney, K. R., Patarasuk, R., Liang, J., Song, Y., O’keeffe, D., Rao, P., Whetstone, J. R., Duren, R. M., Eldering, A., and Miller, C.: The Hestia fossil fuel CO2 emissions data product for the Los Angeles megacity (Hestia-LA), Earth Syst. Sci. Data, 11, 1309–1335, https://doi.org/10.5194/essd-11-1309-2019, 2019b.

Gurney, K. R., Liang, J., Roest, G., Song, Y., Mueller, K., and Lauvaux, T.: Under-reporting of greenhouse gas emissions in U.S. cities, Nat. Commun., 12, https://doi.org/10.1038/s41467-020-20871-0, 2021.

Hamilton, S. D., Wu, D., Johnson, M. S., Turner, A. J., Fischer, M. L., Dadheech, N., and Jeong, S.: Estimating Carbon Dioxide Emissions in Two California Cities Using Bayesian Inversion and Satellite Measurements, Geophys. Res. Lett., 51, https://doi.org/10.1029/2024GL111150, 2024.

Hakkarainen, J., Ialongo, I., and Tamminen, J.: Direct space-based observations of anthropogenic CO2 emission areas from OCO-2, Geophys. Res. Lett., 43, 11400-11406, https://doi.org/10.1002/2016GL070885, 2016.

Hedelius, J. K., Liu, J., Oda, T., Maksyutov, S., Roehl, C. M., Iraci, L. T., Podolske, J. R., Hillyard, P. W., Liang, J., Gurney, K. R., Wunch, D., and Wennberg, P. O.: Southern California megacity CO2, CH4, and CO flux estimates using ground-and space-based remote sensing and a Lagrangian model, Atmos. Chem. Phys., 18, 16271–16291, https://doi.org/10.5194/acp-18-16271-2018, 2018.

Hollingsworth, A. and Lönnberg, P.: The statistical structure of short-range forecast errors as determined from radiosonde data. Part I: The wind field, Tellus A, 38A, 111–136, https://doi.org/10.1111/j.1600-0870.1986.tb00460.x, 1986.

IEA: Energy and Climate Change, World Energy Outlook Special Report, https://www.iea.org/reports/energy-and-climate-change, 2015.

IPCC: Summary for Policymakers, in: Global Warming of 1.5 °C. An IPCC Special Report on the impacts of global warming of 1.5 °C above pre-industrial levels and related global greenhouse gas emission pathways, in the context of strengthening the global response to the threat of climate change, sustainable development, and efforts to eradicate poverty, edited by: Masson-Delmotte, V., Zhai, P., Pörtner, H.-O., Roberts, D., Skea, J., Shukla, P. R., Pirani, A., Moufouma-Okia, W., Péan, C., Pidcock, R., Connors, S., Matthews, J. B. R., Chen, Y., Zhou, X., Gomis, M. I., Lonnoy, E., Maycock, T., Tignor, M., and Waterfield, T., Cambridge University Press, Cambridge, UK and New York, NY, USA, 3–24, https://doi.org/10.1017/9781009157940.001, 2018.

IPCC: 2019 Refinement to the 2006 IPCC Guidelines for National Greenhouse Gas Inventories, edited by: Calvo Buendia, E., Tanabe, K., Kranjc, A., Baasansuren, J., Fukuda, M., Ngarize, S., Osako, A., Pyrozhenko, Y., Shermanau, P., and Federici, S., IPCC, 2019.

IPCC: Sections, in: Climate Change 2023: Synthesis Report. Contribution of Working Groups I, II and III to the Sixth Assessment Report of the Intergovernmental Panel on Climate Change, edited by: Core Writing Team, Lee, H., and Romero, J., IPCC, Geneva, Switzerland, 35–115, https://doi.org/10.59327/IPCC/AR6-9789291691647, 2023.

Janardanan, R., Maksyutov, S., Oda, T., Saito, M., Kaiser, J. W., Ganshin, A., Stohl, A., Matsunaga, T., Yoshida, Y., and Yokota, T.: Comparing GOSAT observations of localized CO2 enhancements by large emitters with inventory-based estimates, Geophys. Res. Lett., 43, 3486–3493, https://doi.org/10.1002/2016GL067843, 2016.

Kaminski, T., Scholze, M., Rayner, P., Houweling, S., Voßbeck, M., Silver, J., Lama, S., Buchwitz, M., Reuter, M., Knorr, W., Chen, H. W., Kuhlmann, G., Brunner, D., Dellaert, S., Denier van der Gon, H., Super, I., Löscher, A., and Meijer, Y.: Assessing the Impact of Atmospheric CO2 and NO2 Measurements From Space on Estimating City-Scale Fossil Fuel CO2 Emissions in a Data Assimilation System, Front. Remote Sens., 3, 1–21, https://doi.org/10.3389/frsen.2022.887456, 2022.

Kiel, M., Eldering, A., Roten, D. D., Lin, J. C., Feng, S., Lei, R., Lauvaux, T., Oda, T., Roehl, C. M., Blavier, J. F., and Iraci, L. T.: Urban-focused satellite CO2 observations from the Orbiting Carbon Observatory-3: A first look at the Los Angeles megacity, Remote Sens. Environ., 258, 112314, https://doi.org/10.1016/j.rse.2021.112314, 2021.

Korea Forest Service: Statistical Yearbook of Forestry, 2021.

Korean Statistical Information Service: http://kosis.kr/.

Kort, E. A., Frankenberg, C., Miller, C. E., and Oda, T.: Space-based observations of megacity carbon dioxide, Geophys. Res. Lett., 39, 1–5, https://doi.org/10.1029/2012GL052738, 2012.

Kunik, L., Mallia, D. V., Gurney, K. R., Mendoza, D. L., Oda, T., and Lin, J. C.: Bayesian inverse estimation of urban CO2 emissions: Results from a synthetic data simulation over Salt Lake City, UT, Elem. Sci. Anthr., 7, 1–16, https://doi.org/10.1525/elementa.375, 2019.

Labzovskii, L. D., Jeong, S.-J., and Parazoo, N. C.: Working towards confident spaceborne monitoring of carbon emissions from cities using Orbiting Carbon Observatory-2, Remote Sens. Environ., 233, 111359, https://doi.org/10.1016/j.rse.2019.111359, 2019.

Lauvaux, T., Miles, N. L., Deng, A., Richardson, S. J., Cambaliza, M. O., Davis, K. J., Gaudet, B., Gurney, K. R., Huang, J., O'Keefe, D., Song, Y., Karion, A., Oda, T., Patarasuk, R., Razlivanov, I., Sarmiento, D., and Wu, K.: High-resolution atmospheric inversion of urban CO2 emissions during the dormant season of the Indianapolis Flux Experiment (INFLUX), J. Geophys. Res. Atmos., 121, 5213–5236, https://doi.org/10.1002/2015JD024473, 2016.

Lian, J., Lauvaux, T., Utard, H., Bréon, F. M., Broquet, G., Ramonet, M., Laurent, O., Albarus, I., Cucchi, K., and Ciais, P.: Assessing the Effectiveness of an Urban CO2 Monitoring Network over the Paris Region through the COVID-19 Lockdown Natural Experiment, Environ. Sci. Technol., 56, 2153–2162, https://doi.org/10.1021/acs.est.1c04973, 2022.

Lian, J., Lauvaux, T., Utard, H., Bréon, F. M., Broquet, G., Ramonet, M., Laurent, O., Albarus, I., Chariot, M., Kotthaus, S., Haeffelin, M., Sanchez, O., Perrussel, O., Denier Van Der Gon, H. A., Dellaert, S. N. C., and Ciais, P.: Can we use atmospheric CO2 measurements to verify emission trends reported by cities? Lessons from a 6-year atmospheric inversion over Paris, Atmos. Chem. Phys., 23, 8823–8835, https://doi.org/10.5194/acp-23-8823-2023, 2023.

Lin, J. C., Gerbig, C., Wofsy, S. C., Andrews, A. E., Daube, B. C., Davis, K. J., and Grainger, C. A.: A near-field tool for simulating the upstream influence of atmospheric observations: The Stochastic Time-Inverted Lagrangian Transport (STILT) model, J. Geophys. Res. Atmos., 108, https://doi.org/https://doi.org/10.1029/2002JD003161, 2003.

Lönnberg, P. and Hollingsworth, A.: The statistical structure of short-range forecast errors as determined from radiosonde data. Part II: The covariance of height and wind errors, Tellus A, 38A, 137–161, https://doi.org/10.1111/j.1600-0870.1986.tb00461.x, 1986.

Lopez-Coto, I., Ren, X., Salmon, O. E., Karion, A., Shepson, P. B., Dickerson, R. R., Stein, A., Prasad, K., and Whetstone, J. R.: Wintertime CO2, CH4, and CO Emissions Estimation for the Washington, DC–Baltimore Metropolitan Area Using an Inverse Modeling Technique, Environ. Sci. Technol., 54, 2606–2614, https://doi.org/10.1021/acs.est.9b06619, 2020.

Mallia, D. V., Mitchell, L. E., Kunik, L., Fasoli, B., Bares, R., Gurney, K. R., Mendoza, D. L., and Lin, J. C.: Constraining Urban CO2 Emissions Using Mobile Observations from a Light Rail Public Transit Platform, Environ. Sci. Technol., 54, 15613–15621, https://doi.org/10.1021/acs.est.0c04388, 2020.

McKain, K., Wofsy, S. C., Nehrkorn, T., Eluszkiewicz, J., Ehleringer, J. R., and Stephens, B. B.: Assessment of ground-based atmospheric observations for verification of greenhouse gas emissions from an urban region, Proc. Natl. Acad. Sci. U.S.A., 109, 8423–8428, https://doi.org/10.1073/pnas.1116645109, 2012.

Moran, D., Kanemoto, K., Jiborn, M., Wood, R., Többen, J., and Seto, K. C.: Carbon footprints of 13 000 cities, Environ. Res. Lett., 13, 064041, https://doi.org/10.1088/1748-9326/aac72a, 2018.

Mueller, K. L., Lauvaux, T., Gurney, K. R., Roest, G., Ghosh, S., Gourdji, S. M., Karion, A., DeCola, P., and Whetstone, J.: An emerging GHG estimation approach can help cities achieve their climate and sustainability goals, Environ. Res. Lett., 16, https://doi.org/10.1088/1748-9326/ac0f25, 2021.

Nalini, K., Lauvaux, T., Abdallah, C., Lian, J., Ciais, P., Utard, H., Laurent, O., and Ramonet, M.: High-Resolution Lagrangian Inverse Modeling of CO2 Emissions Over the Paris Region During the First 2020 Lockdown Period, J. Geophys. Res. Atmos., 127, 1–26, https://doi.org/10.1029/2021JD036032, 2022.

Nassar, R., Napier-Linton, L., Gurney, K. R., Andres, R. J., Oda, T., Vogel, F. R., and Deng, F.: Improving the temporal and spatial distribution of co2 emissions from global fossil fuel emission data sets, J. Geophys. Res. Atmos., 118, 917–933, https://doi.org/10.1029/2012JD018196, 2013.

Nehrkorn, T., Eluszkiewicz, J., Wofsy, S. C., Lin, J. C., Gerbig, C., Longo, M., and Freitas, S.: Coupled weather research and forecasting-stochastic time-inverted lagrangian transport (WRF-STILT) model, Meteorol. Atmos. Phys., 107, 51–64, https://doi.org/10.1007/s00703-010-0068-x, 2010.

Thoning, K.W., P.P. Tans, and W.D. Komhyr: Atmospheric carbon dioxide at Mauna Loa Observatory: 2. Analysis of the NOAA GMCC data, 1974–1985, J. Geophys. Res. Atmos., 94, 8549–8565, https://doi.org/10.1029/JD094iD06p08549, 1989.

Oda, T. and Maksyutov, S.: A very high-resolution (1km×1 km) global fossil fuel CO2 emission inventory derived using a point source database and satellite observations of nighttime lights, Atmos. Chem. Phys., 11, 543–556, https://doi.org/10.5194/acp-11-543-2011, 2011.

Oda, T., Maksyutov, S., and Andres, R. J.: The Open-source Data Inventory for Anthropogenic CO2, version 2016 (ODIAC2016): a global monthly fossil fuel CO2 gridded emissions data product for tracer transport simulations and surface flux inversions, Earth Syst. Sci. Data, 10, 87–107, https://doi.org/10.5194/essd-10-87-2018, 2018.

Oda, T., Bun, R., Kinakh, V., Topylko, P., Halushchak, M., Marland, G., Lauvaux, T., Jonas, M., Maksyutov, S., Nahorski, Z., Lesiv, M., Danylo, O., and Horabik-Pyzel, J.: Errors and uncertainties in a gridded carbon dioxide emissions inventory, Mitig. Adapt. Strateg. Glob. Chang., 24, 1007–1050, https://doi.org/10.1007/s11027-019-09877-2, 2019.

Ohyama, H., Frey, M. M., Morino, I., Shiomi, K., Nishihashi, M., Miyauchi, T., Yamada, H., Saito, M., Wakasa, M., Blumenstock, T., and Hase, F.: Anthropogenic CO2 emission estimates in the Tokyo metropolitan area from ground-based CO2 column observations, Atmos. Chem. Phys., 23, 15097–15119, https://doi.org/10.5194/acp-23-15097-2023, 2023.

Palermo, V., Bertoldi, P., Crippa, M., Franco, C., Monforti-Ferrario, F., and Pisoni, E.: Uncovering divergences and potential gaps in local greenhouse gases emissions accounting and aggregation, Curr. Res. Environ. Sustain., 8, 100263, https://doi.org/10.1016/j.crsust.2024.100263, 2024.

Park, C., Jeong, S., Park, H., Woo, J.-H., Sim, S., Kim, J., Son, J., Park, H., Shin, Y., Shin, J.-H., Kwon, S.-M., and Lee, W.-Y.: Challenges in Monitoring Atmospheric CO2 Concentrations in Seoul Using Low-Cost Sensors, Asia-Pacific J. Atmos. Sci., 57, 547–553, https://doi.org/10.1007/s13143-020-00213-2, 2021.

Park, C., Jeong, S., Park, H., Sim, S., Hong, J., and Oh, E.: Comprehensive assessment of vertical variations in urban atmospheric CO2 concentrations by using tall tower measurement and an atmospheric transport model, Urban Clim., 45, 101283, https://doi.org/10.1016/j.uclim.2022.101283, 2022.

Park, H., Jeong, S., Park, H., Labzovskii, L. D., and Bowman, K. W.: An assessment of emission characteristics of Northern Hemisphere cities using spaceborne observations of CO2, CO, and NO2, Remote Sens. Environ., 254, 112246, https://doi.org/10.1016/j.rse.2020.112246, 2021.

Patarasuk, R., Gurney, K. R., O'Keeffe, D., Song, Y., Huang, J., Rao, P., Buchert, M., Lin, J. C., Mendoza, D., and Ehleringer, J. R.: Urban high-resolution fossil fuel CO2 emissions quantification and exploration of emission drivers for potential policy applications, Urban Ecosyst., 19, 1013–1039, https://doi.org/10.1007/s11252-016-0553-1, 2016.

Pisso, I., Patra, P., Takigawa, M., Machida, T., Matsueda, H., and Sawa, Y.: Assessing Lagrangian inverse modelling of urban anthropogenic CO2 fluxes using in situ aircraft and ground-based measurements in the Tokyo area, Carbon Balance Manag., 14, 1–23, https://doi.org/10.1186/s13021-019-0118-8, 2019.

Pitt, J. R., Lopez-Coto, I., Hajny, K. D., Tomlin, J., Kaeser, R., Jayarathne, T., Stirm, B. H., Floerchinger, C. R., Loughner, C. P., Gately, C. K., Hutyra, L. R., Gurney, K. R., Roest, G. S., Liang, J., Gourdji, S., Karion, A., Whetstone, J. R., and Shepson, P. B.: New York City greenhouse gas emissions estimated with inverse modeling of aircraft measurements, Elementa, 10, 1–13, https://doi.org/10.1525/elementa.2021.00082, 2022.

Robinson, M. and Shine, T.: Achieving a climate justice pathway to 1.5 °c, Nat. Clim. Chang., 8, 564–569, https://doi.org/10.1038/s41558-018-0189-7, 2018.

Roten, D., Lin, J. C., Das, S., and Kort, E. A.: Constraining Sector-Specific CO2 Fluxes Using Space-Based XCO2 Observations Over the Los Angeles Basin, Geophys. Res. Lett., 50, 1–11, https://doi.org/10.1029/2023GL104376, 2023.

Ruckstuhl, A. F., Henne, S., Reimann, S., Steinbacher, M., Vollmer, M. K., O'Doherty, S., Buchmann, B., and Hueglin, C.: Robust extraction of baseline signal of atmospheric trace species using local regression, Atmos. Meas. Tech., 5, 2613–2624, https://doi.org/10.5194/amt-5-2613-2012, 2012.

Rutherford, I. D.: Data Assimilation by Statistical Interpolation of Forecast Error Fields, J. Atmos. Sci., 29, 809–815, https://doi.org/10.1175/1520-0469(1972)029<0809:DABSIO>2.0.CO;2, 1972.

Sargent, M., Barrera, Y., Nehrkorn, T., Hutyra, L. R., Gately, C. K., Jones, T., Mckain, K., Sweeney, C., Hegarty, J., Hardiman, B., Wang, J. A., and Wofsy, S. C.: Correction: Anthropogenic and biogenic CO2 fluxes in the Boston urban region (Proceedings of the National Academy of Sciences of the United States of America (2018) 115 (7491-7496) DOI: 10.1073/pnas.1803715115), Proc. Natl. Acad. Sci. U. S. A., 115, E9507, https://doi.org/10.1073/pnas.1815348115, 2018.

Schneising, O., Heymann, J., Buchwitz, M., Reuter, M., Bovensmann, H., and Burrows, J. P.: Anthropogenic carbon dioxide source areas observed from space: Assessment of regional enhancements and trends, Atmos. Chem. Phys., 13, 2445–2454, https://doi.org/10.5194/acp-13-2445-2013, 2013.

Seoul Metropolitan Government: 2050 Seoul Climate Action Plan, 2021.

Sim, S., Jeong, S., Park, H., Park, C., Kwak, K. H., Lee, S. B., Kim, C. H., Lee, S., Chang, J. S., Kang, H., and Woo, J. H.: Co-benefit potential of urban CO2 and air quality monitoring: A study on the first mobile campaign and building monitoring experiments in Seoul during the winter, Atmos. Pollut. Res., 11, 1963–1970, https://doi.org/10.1016/j.apr.2020.08.009, 2020.

Silva, S. and Arellano, A.: Characterizing Regional-Scale Combustion Using Satellite Retrievals of CO, NO2 and CO2, Remote Sens., 9, 744, https://doi.org/10.3390/rs9070744, 2017.

Sim, S., Jeong, S., Park, C., Shin, J., Kim, I., Ban, S., and Lim, C.-S.: Designing an Atmospheric Monitoring Network to Verify National CO2 Emissions, Asia-Pacific J. Atmos. Sci., 60, 131–141, https://doi.org/10.1007/s13143-023-00343-3, 2023.

Skamarock, W. C. and Klemp, J. B.: A time-split nonhydrostatic atmospheric model for weather research and forecasting applications, J. Comput. Phys., 227, 3465–3485, https://doi.org/10.1016/j.jcp.2007.01.037, 2008.

Staufer, J., Broquet, G., Bréon, F. M., Puygrenier, V., Chevallier, F., Xueref-Rémy, I., Dieudonné, E., Lopez, M., Schmidt, M., Ramonet, M., Perrussel, O., Lac, C., Wu, L., and Ciais, P.: The first 1-year-long estimate of the Paris region fossil fuel CO2 emissions based on atmospheric inversion, Atmos. Chem. Phys., 16, 14703–14726, https://doi.org/10.5194/acp-16-14703-2016, 2016.

Tarantola, A.: Inverse Problem Theory Methods for Data Fitting and Model Parameter Estimation, Elsevier Science, 1987.

UN-DESA: World Urbanization Prospects, 197–236, 2018.

WRI, C40 Cities, and ICLEI: Global Protocol for Community-Scale Greenhouse Gas Emission Inventories: An Accounting and Reporting Standard for Cities (GPC), World Resour. Inst., 1–176, 2014.

Wu, D., Lin, J. C., Fasoli, B., Oda, T., Ye, X., Lauvaux, T., Yang, E. G., and Kort, E. A.: A Lagrangian approach towards extracting signals of urban CO2 emissions from satellite observations of atmospheric column CO2 (XCO2): X-Stochastic Time-Inverted Lagrangian Transport model ("X-STILT v1"), Geosci. Model Dev., 11, 4843–4871, https://doi.org/10.5194/gmd-11-4843-2018, 2018.

Yadav, V. and Michalak, A. M.: Improving computational efficiency in large linear inverse problems: an example from carbon dioxide flux estimation, Geosci. Model Dev., 6, 583–590, https://doi.org/10.5194/gmd-6-583-2013, 2013.

Ye, X., Lauvaux, T., Kort, E. A., Oda, T., Feng, S., Lin, J. C., Yang, E. G., and Wu, D.: Constraining Fossil Fuel CO2 Emissions From Urban Area Using OCO-2 Observations of Total Column CO2, J. Geophys. Res. Atmos., 125, e2019JD030528, https://doi.org/10.1029/2019JD030528, 2020.

Zhao, C., Andrews, A. E., Bianco, L., Eluszkiewicz, J., Hirsch, A., MacDonald, C., Nehrkorn, T., and Fischer, M. L.: Atmospheric inverse estimates of methane emissions from Central California, J. Geophys. Res. Atmos., 114, 1–13, https://doi.org/10.1029/2008JD011671, 2009.